Seismic diffusivity and the influence of heterogeneity on injection-induced seismicity

Ryan Haagenson[1,2] **and Harihar Rajaram**[1,2]

[1]Environmental Health and Engineering, Johns Hopkins University, 615 N Wolfe St, Baltimore, MD, 21205, USA

[2]Civil, Environmental, and Architectural Engineering, University of Colorado Boulder, 1111 Engineering Dr, 422 UCB, Boulder, CO, 80309, USA

Key Points:

- We present numerical simulations to investigate the influence of heterogeneous hydraulic properties on induced seismicity
- We find the seismic diffusivity associated with propagation of induced seismicity to be distinct from the effective hydraulic diffusivity
- The seismic diffusivity can be an order of magnitude larger than the effective hydraulic diffusivity in fractured rock

Corresponding author: Ryan Haagenson, rhaagenson@jhu.edu

Abstract

The spatiotemporal patterns of injection-induced seismicity (IIS) are commonly interpreted with the concept of a triggering front, which propagates in a diffusion-like manner with an associated diffusivity parameter. Here, we refer to this diffusivity as the "seismic diffusivity". Several previous studies implicitly assume that seismic diffusivity is equivalent to the effective hydraulic diffusivity of the subsurface, which describes the behavior of the mean pressure field in heterogeneous porous media. Seismicity-based approaches for hydraulic characterization or simulations of IIS using domains of homogeneous equivalent porous media are implicitly based on this assumed equivalence. However, seismicity is expected to propagate with the threshold triggering pressure, and thus not be controlled by the evolution of the mean pressure field. We present numerical simulations of fluid injection to compare the seismic and effective hydraulic diffusivities in heterogeneous formations (including fractured rock). The numerical model combines uncoupled, linear pressure diffusion with the Mohr-Coulomb failure criterion to simulate IIS. We demonstrate that connected pathways of relatively high hydraulic diffusivity in heterogeneous media (particularly in fractured rock domains) allow the threshold triggering pressure to propagate more rapidly than predicted by the effective hydraulic diffusivity. As a result, the seismic diffusivity is greater than the effective hydraulic diffusivity in heterogeneous porous media, possibly by an order of magnitude or more. Additionally, we present a case study of IIS near Soultz-sous-Forêts where seismic diffusivity is found to be at least one order of magnitude larger than the effective hydraulic diffusivity.

1 Introduction

The injection of fluid into the subsurface is a common practice in several industries such as geothermal energy production, wastewater disposal, or hydraulic stimulation. In some cases, changes to the subsurface fluid pressure distribution or stress state may trigger seismic events, with potential risks to the nearby population and infrastructure depending on the magnitude of the induced seismicity (Chase et al., 2019; Ellsworth, 2013; Majer et al., 2012; Rutqvist et al., 2014; Weingarten et al., 2015). The first recorded incident of injection induced seismicity (IIS) was near Denver, Colorado in 1962 (Healy et al., 1968). The authors concluded that an increase in the fluid pressure within the injection formation led to a decrease in the effective normal stress acting along previously dormant faults and fractures, thus prompting increased seismic activity in the area. In the United States, IIS has been mostly associated with the disposal of coproduced wastewater from oil and gas operations (EPA, 2016; Weingarten et al., 2015); although, IIS is common in numerous other industries, including geologic carbon sequestration and geothermal energy (Cataldi et al., 2016; Cuenot et al., 2008; Majer et al., 2012; Riffault et al., 2018). Several studies have investigated the behavior and physical mechanisms of IIS in numerical, statistical, and field studies (Chang & Segall, 2016; Hajati et al., 2015; Langenbruch & Zoback, 2016; Rudnicki, 1986; Segall & Lu, 2015; Shapiro et al., 1997; Talwani & Acree, 1985).

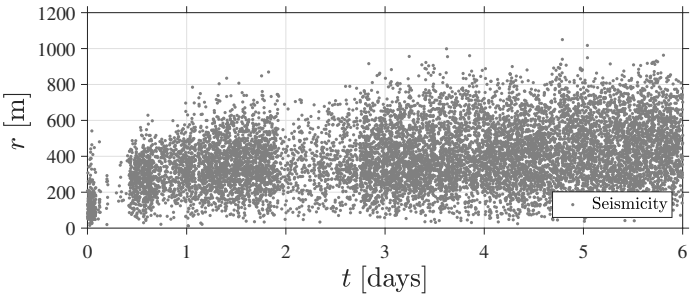

Figure 1. The recorded seismic events from the 2000 fluid injection experiment near Soultz-sous-Forêts, France plotted as r-t plot (Leptokaropoulos et al., 2019).

Complex changes to the subsurface stress state – either through poroelastic effects or static stress transfers – certainly impact the behavior of seismicity during fluid injection (Catalli et al., 2016; Chang & Segall, 2016; Chang & Yoon, 2020; Haagenson et al., 2020; Jha & Juanes, 2014; Rutqvist et al., 2013; Schoenball et al., 2012; Segall & Lu, 2015; Zhai & Shirzaei, 2018; Zhai et al., 2019). However, most studies assume that the decrease of effective normal stress acting along a fault or fracture due to the increase of pore fluid pressure from fluid injection is the dominant physical mechanism causing seismicity (Brown et al., 2017; Dempsey & Riffault, 2019; Hummel & Shapiro, 2013; Keranen et al., 2014; Langenbruch et al., 2018; Nakai et al., 2017; Shapiro et al., 1997, 2002; Shapiro & Dinske, 2009b; Shapiro, 2015; Rothert & Shapiro, 2003; Talwani & Acree, 1985). If we neglect changes to the subsurface stress state, the triggering of seismic events during fluid injection is expected to be predominantly controlled by fluid flow. Here, we model fluid flow using an uncoupled diffusion equation of fluid pressure, based on the clear precedence in the classical theory of groundwater flow (Bear, 1972; Charbeneau, 2006; De Marsily, 1986; Verruijt, 2013) and of linear poroelasticity in cases of irrotational deformation (Cleary, 1977; Rice & Cleary, 1976; Rudnicki, 1986).

At sites prone to IIS, seismic events are observed to occur at increasingly larger radial distances from the injection location as time progresses. A convenient approach to understanding the spatiotemporal behavior of IIS is to plot the distance between the injection location and the seismic event hypocenter against the event occurrence time. These plots are commonly referred to as r-t plots. As an example, the recorded seismic dataset from the fluid injection experiment near Soultz-sous-Forêts, France from the year 2000 is shown as an r-t plot in Figure 1 (Delepine et al., 2004; Leptokaropoulos et al., 2019). We will further discuss the results of this fluid injection experiment in Section 4.

Several previous studies have employed r-t plots to investigate the diffusive propagation of the so-called triggering front (Antonioli et al., 2005; Chen et al., 2012; Ingebritsen & Manning, 2010; Goebel et al., 2017; Goertz-Allmann et al., 2017; Haffener et al., 2018; Hummel & Shapiro, 2013; Shapiro et al., 1997, 2002; Shapiro & Dinske, 2009a; Yong et al., 2018; Yu et al., 2019). In the most general terms, the triggering front is the three-

dimensional surface propagating away from the injection location (which need not be radially symmetric) at which the onset of seismicity occurs (Rothert & Shapiro, 2003; Shapiro et al., 1997; Shapiro & Müller, 1999; Shapiro et al., 2002; Shapiro, 2015). If we assume that the onset of seismicity is induced by a threshold triggering pressure increment (p_t) (Dempsey & Riffault, 2019; Gischig & Wiemer, 2013; Goebel et al., 2017; Keranen et al., 2014; Shapiro, 2015), then the triggering front may be alternatively viewed as the isobaric surface with a pressure increment value equal to p_t. While r-t plots directionally aggregate the three-dimensional seismic dataset and thus only reflect variations of seismicity in the radial direction, they are still helpful for tracking the location of the triggering front. As previous studies have shown (Delepine et al., 2004; Shapiro et al., 1997, 2002; Shapiro, 2015), the location of the triggering front can be approximately identified by the upper envelope of the seismic data cluster in an r-t plot such as Figure 1, if the subsurface is assumed to be homogeneous and isotropic. This represents the farthest radial distance from the injection location where seismicity has occurred at any given time.

It is well established that the propagation of seismicity and the triggering front (as observed in r-t plots) is approximately described by a diffusion-like process (Shapiro et al., 1997; Shapiro, 2015; Talwani & Acree, 1985). As such, expressions describing the diffusive propagation of the triggering front can be fit to the upper envelope of the seismic data cluster, producing an estimate of diffusivity (Delepine et al., 2004; Hummel & Müller, 2009; Hummel & Shapiro, 2012, 2013; Rothert & Shapiro, 2003; Segall & Lu, 2015; Shapiro et al., 1997; Shapiro & Müller, 1999; Shapiro et al., 2002; Shapiro & Dinske, 2009a, 2009b; Shapiro, 2015). For clarity, we refer to this estimate of diffusivity as the "seismic diffusivity", borrowing the term from Talwani and Acree (1985). There, the authors suggested that estimates of seismic diffusivity (associated with the spatiotemporal patterns of IIS) are in fact accurate estimates of the effective hydraulic diffusivity of the injection formation. If true, this indicates that methods for estimating seismic diffusivity are in fact seismicity-based approaches for subsurface hydraulic characterization. Since Talwani and Acree (1985), numerous other studies have also implicitly assumed that seismic diffusivity and effective hydraulic diffusivity are equivalent, and thus the term "seismic diffusivity" is not widely used (Haagenson et al., 2018; Haagenson & Rajaram, 2020).

The seismic diffusivity and effective hydraulic diffusivity are no doubt equivalent in homogeneous and isotropic porous media, where isobaric surfaces (including the triggering front) will be radially symmetric. When employing r-t plots, the location of the triggering front is described as a single radial distance from the injection location, which hence implicitly assumes that the subsurface is homogeneous and isotropic. Indeed, most studies of the spatiotemporal patterns of IIS, using both analytical models (Antonioli et al., 2005; Chen et al., 2012; Goebel et al., 2017; Goertz-Allmann et al., 2017; Haffener et al., 2018; Hummel & Shapiro, 2012, 2013; Ingebritsen & Manning, 2010; Segall & Lu, 2015; Shapiro et al., 1997; Shapiro & Dinske, 2009a, 2009b; Yong et al., 2018; Yu et al., 2019) and numerical models (Brown et al., 2017; Catalli et al., 2016; Dempsey & Rif-

fault, 2019; Keranen et al., 2014; Langenbruch & Zoback, 2016; Langenbruch et al., 2018; Pollyea et al., 2019; Riffault et al., 2018), assume a homogeneous injection formation.

An important question that arises is whether the aforementioned equivalence between seismic diffusivity and effective hydraulic diffusivity holds in a heterogeneous porous medium. Fluid flow and pressure diffusion in subsurface formations are influenced by heterogeneity of hydraulic and mechanical properties in natural earth materials; this influence has been investigated in an extensive body of literature over the last 40 years and synthesized in several textbooks (Dagan, 1989; Gelhar, 1993; Zhang, 2001). When heterogeneity is represented as a spatially correlated random field with a well-defined correlation length, it is generally accepted that (at scales much larger than the correlation length) the behavior of the mean pressure and fluid flux fields can be described by effective permeability and hydraulic diffusivity tensors. Similar frameworks exist for defining block-scale effective conductivities for large grid blocks in field-scale flow models based on the underlying heterogeneity structure (Renard & De Marsily, 1997; Sanchez-Vila et al., 2006; Wen & Gómez-Hernández, 1996) or fracture network topology (Botros et al., 2008; Long et al., 1982; R. Zimmerman & Bodvarsson, 1996). The above body of literature provides a basis for representing flow behavior in heterogeneous media in terms of equivalent homogeneous media with effective properties determined by the spatial structure of heterogeneity. Most field-scale modeling of fluid flow in hydrogeology implicitly adopts this view and only represents material property variations across distinct geological units explicitly. Moreover, field-scale hydraulic tests are commonly interpreted based on analytical solutions for fluid flow in homogeneous media and the properties estimated from these tests are assumed to reflect effective properties (such as the effective permeability) at the test scale (Gelhar, 1993). In radial flow, theoretical and computational analyses in heterogeneous media (e.g. Naff (1991) or Guadagnini et al. (2003)) demonstrate that apparent conductivities approach constant values equal to the effective conductivities within a few correlation lengths from the well. Similarly, analytical and numerical modeling studies of IIS and frameworks for interpreting the spatiotemporal patterns of IIS may often be viewed as implicitly adopting equivalent homogeneous representations of hydraulic properties (Brown et al., 2017; Catalli et al., 2016; Dempsey & Riffault, 2019; Keranen et al., 2014; Langenbruch & Zoback, 2016; Langenbruch et al., 2018; Pollyea et al., 2019; Riffault et al., 2018; Segall & Lu, 2015; Shapiro et al., 1997; Shapiro & Müller, 1999; Shapiro & Dinske, 2009a, 2009b; Shapiro, 2015). As mentioned above, these approaches rely on the assumed equivalence between the seismic diffusivity and effective hydraulic diffusivity of the subsurface (Haagenson et al., 2018; Haagenson & Rajaram, 2020).

Our specific goal in this paper is to demonstrate that in highly heterogeneous porous media, there is a clear distinction between the seismic diffusivity and the effective hydraulic diffusivity. In reality, the triggering front is not radially symmetric for cases of heterogeneous domains. This is because pressure increments are expected to propagate preferentially through pathways of relatively high hydraulic diffusivity in heterogeneous media. As a result, the farthest radial distance to which the threshold triggering pres-

sure increment propagates (which we denote as $r_{max}(p = p_t)$ and is synonymous with the triggering front in the context of r-t plots) will be farther than the radial distance at which the directionally averaged pressure increment equals the threshold triggering pressure increment (which we denote as $r(p_{avg} = p_t)$ and propagates according to the effective hydraulic diffusivity). Therefore, the triggering front observed in r-t plots will propagate more rapidly than predicted by the effective hydraulic diffusivity. Put another way, seismicity will propagate more rapidly in a realistic, heterogeneous domain than it would in an equivalent homogeneous domain that employs the effective hydraulic diffusivity, since the latter would inevitably underestimate the farthest radial distance reached by the threshold triggering pressure increment (p_t) at any given time. We investigate this possible distinction, the degree to which these two quantities may differ, and what subsurface conditions may exacerbate the difference.

We investigate these questions using numerical simulations of fluid flow and induced seismicity. After providing a description of the computational framework (in Section 2), we present results of simulated fluid injection and induced seismicity in two different types of heterogeneous domains: smoothly varying fields of random hydraulic diffusivity derived using Sequential Gaussian Simulation (i.e. SGS domains described in Section 2.1) and three-dimensional discrete fracture networks in rock matrix (i.e. DFNM domains described in Section 2.2). In Section 4, we present a case study of the fluid injection experiment near Soultz-sous-Forêts, France from the year 2000, which further illustrates the potential distinction between the seismic and effective hydraulic diffusivity (Dezayes et al., 2010; Dorbath et al., 2009; Genter et al., 2010; Meller & Ledésert, 2017).

2 Computational Framework

Here, we investigate the behavior of fluid flow and IIS in correlated random fields of hydraulic diffusivity as well as a domain of highly fractured rock. The random fields are generated using a Sequential Gaussian Simulation (SGS) algorithm, producing a smoothly varying field of hydraulic diffusivity (which are a common but relatively simple representation of heterogeneity in the subsurface) (Müller & Schüler, 2020). We refer to the domain of highly fractured rock as a discrete fracture network and matrix (DFNM) domain, because we explicitly model fluid flow in both the fracture network and surrounding rock matrix (Birdsell et al., 2018; Haagenson et al., 2018; Haagenson & Rajaram, 2020). This is a more realistic representation of the kind of formation in which IIS typically occurs.

For simplicity, we consider only heterogeneous media with large-scale, isotropic effective permeability and diffusivity tensors (i.e. statistically isotropic correlation structures in the SGS domains and uniform orientation distributions for fractures in the DFNM domains). These models are readily generalizable to represent large-scale anisotropy resulting from either anisotropic spatial correlation in the SGS domains or non-uniform orientation distributions (e.g. families of similarly aligned fractures) in the DFNM domains. However, our purpose here is mainly to illustrate the influence of heterogeneity

on the propagation of the triggering front, which is expected to occur with or without anisotropy.

We model fluid flow through a porous medium in response to a point source of fluid injection based on the classical pressure diffusion equation (Bear, 1972; Charbeneau, 2006; Cleary, 1977; De Marsily, 1986; Rice & Cleary, 1976; Rudnicki, 1986; Verruijt, 2013), given as

$$\rho_f \left(\phi\beta_f + \beta_m\right) \frac{\partial p}{\partial t} - \nabla \cdot \left(\frac{\rho_f \kappa}{\mu} \nabla p\right) = Q_m \tag{1}$$

where ρ_f is the fluid density, ϕ is the porosity of the porous medium, β_f and β_m are the compressibilities of the fluid and porous medium respectively, p is the increment of pore fluid pressure (with respect to the initial, static pressure distribution), κ is the intrinsic permeability of the porous medium, μ is the dynamic viscosity of the fluid, and Q_m is the source or sink of fluid mass. Although some of these parameters (particularly permeability) can exhibit pressure dependence, we use constant parameter values such that equation (1) becomes a linear diffusion equation. Our goal is to highlight the influence of heterogeneity on patterns of IIS within the framework of linear diffusion. We intend to investigate the nuanced behavior of nonlinear fluid flow and IIS in future work. In this form, equation (1) represents a diffusion equation of pressure increment, where the well-known hydraulic diffusivity (Bear, 1972; De Marsily, 1986) is defined as

$$D_h = \frac{\kappa}{\mu \left(\phi\beta_f + \beta_m\right)}. \tag{2}$$

Flow through porous media (either in the SGS domain or in the rock matrix portion of the DFNM domain) is governed by equation (1). For the fractures, the model employs an alternative form of the general fracture flow equation:

$$\frac{\partial \left(\rho_f b\right)}{\partial t} - \nabla \cdot \left(\frac{\rho_f b^3}{12\mu} \nabla p\right) = Q_f - L_m \tag{3}$$

where b is the fracture aperture, Q_f is the source or sink of fluid mass per unit area of the fracture and L_m is the fluid leak-off rate per unit area from the fracture into the surrounding rock matrix (Chaudhuri et al., 2013; Murphy et al., 2004). Equation (3) employs the well-known local cubic law for fracture transmissivity (R. W. Zimmerman & Bodvarsson, 1996). Although there are limitations to the local cubic law at smaller scales, it is widely used in DFN models (Adler et al., 2013; Frampton et al., 2019; J. Hyman et al., 2015) with a constant aperture (b) within individual fractures (which may also be interpreted as the equivalent hydraulic aperture). In Section 2.2.2 below, we further describe how equation 3 can be expressed in the form of a diffusion equation and solved in combination with the pressure diffusion equation in the rock matrix given in equation (1).

Table 1. Summary of fluid injection model parameters.

Parameter	Description	Value	Unit
ρ_f	fluid density	998	kg/m^3
μ	fluid viscosity	$8.9 \cdot 10^{-4}$	$Pa \cdot s$
β_f	fluid compressibility	$4.4 \cdot 10^{-10}$	Pa^{-1}
H_{inj}	depth of injection location	4,000	m
Q	injection rate of fluid	25	m^3/hr
t_e	injection period	12	hours
H_{wt}	depth of water table	100	m
ρ_s	density of overburden	2,300	kg/m^3

For simulations of fluid injection, we have developed a numerical model to solve equations (1) and (3) using FEniCS – a general-purpose, open-source finite element method (FEM) software (Alnæs et al., 2015), which has been previously applied to a wide range of geoscientific problems including subsurface fluid flow and generalized poroelasticity (Haagenson et al., 2020). Each domain used in this study is cubic, with sides measuring two kilometers in length. Fluid is injected at the center vertex of the numerical mesh (as a point source of fluid injection) at a constant rate (Q) of 25 cubic meters per hour for a period (t_e) of 12 hours. These parameters were selected to reflect a realistic scenario of fluid injection (Shapiro et al., 1997, 2005; Shapiro & Dinske, 2009b), while also minimizing potential boundary effects by employing a sufficiently large domain (with domain boundaries located a distance of at least $12\sqrt{D_{eff}t_e}$ away from the injection location, where D_{eff} is the effective hydraulic diffusivity of the heterogeneous domain). The initial condition and all boundary conditions are set to a hydrostatic pressure field. A summary of the parameters used in the numerical simulations (which apply to simulations of both the SGS and DFNM domains) are given in Table 1.

Following the approach of Rinaldi and Nespoli (2017), Catalli et al. (2016), and Shapiro (2015), we track seismicity using a set of weak points, which are seeded randomly within one kilometer of the injection location. Each weak point represents a potential location for seismicity. In the SGS domain, each weak point is randomly assigned a strike and dip angle (to represent a hypothetical fracture at that location), whereas the weak points in the DFNM domain are seeded exclusively along fractures and are assigned the corresponding fracture's strike and dip angle. The weak point triggering pressure increment (p_t^{wp}), which is the increase in fluid pressure above the initial fluid pressure that would trigger a seismic event, is found using the well-known Mohr-Coulomb failure criterion:

$$f\left(\sigma_n - (p_t^{wp} + p_i)\right) - |\tau| \leq 0 \tag{4}$$

where f is the coefficient of static friction of the fracture, p_i is the initial fluid pressure at the weak point, and σ_n and τ are the normal compressive stress and shear stress acting on the fracture respectively. The coefficient of friction is allowed to vary between 0.6 and 0.7 to capture a realistic range of values (Jaeger, 1959; Talwani & Acree, 1985). The initial pressure profile is assumed to be hydrostatic, and is found using a constant fluid density ($\rho_f = 998$ kg/m^3) and a water table located 100 meters below the ground surface. The depth of the fluid injection (H_{inj}) and is stipulated as four kilometers. The stresses σ_n and τ can be found using the expressions

$$\sigma_n = (\boldsymbol{\sigma} \cdot \vec{n}) \cdot \vec{n} \tag{5}$$

and

$$\tau = (\boldsymbol{\sigma} \cdot \vec{n}) \times \vec{n} \tag{6}$$

where $\boldsymbol{\sigma}$ is the local stress tensor and $\vec{n}$ is the normal vector of the fracture plane. We have assumed that the local stress tensor is defined by a normal faulting, lithostatic condition where the vertical stress component of $\boldsymbol{\sigma}$ is defined as $\sigma_v = \rho_s g H_{inj}$ and both horizontal components as $\sigma_h = 0.6\sigma_v$ (Zoback, 2010). The rock density of the overburden (ρ_s) is assumed to be 2,300 kilograms per cubic meter.

Commonly, pressure increments associated with induced seismicity are assumed to lie in the range of 0.01 and 0.1 MPa, where a pressure increment less than 0.01 MPa is either not significant enough to trigger seismicity or is often met by processes other than fluid injection (such as background fluid flow or tidal forcing) (Dempsey & Riffault, 2019; Gischig & Wiemer, 2013; Goebel et al., 2017; Keranen et al., 2014; Shapiro, 2015). Thus, weak points with a triggering pressure increment outside this range are removed from the final set of weak points used in the simulation. It is clear then, that the threshold triggering pressure increment associated with the triggering front will in fact be the minimum of the range of weak point triggering pressure increment values (i.e. $p_t = min(p_t^{wp}) =$ 0.01 MPa).

To track seismicity in the numerical simulations, each weak point is evaluated for potential failure in each time step of the simulation. If the local pressure increment due to fluid injection at the weak point location exceeds the weak point triggering pressure increment (indicating that the weak point fails the Mohr-Coulomb criterion), then the weak point's location is recorded as the hypocenter of a seismic event at that given time. This approach results in a synthetic IIS dataset, which allows us to produce r-t plots in order to investigate the spatiotemporal patterns of seismicity and estimate the seismic diffusivity of the heterogeneous domain (following the approach described later in Section 2.4).

The following sections describe the specifics related to the SGS and DFNM domains, including how each domain was generated and spatially discretized, the set of weak points

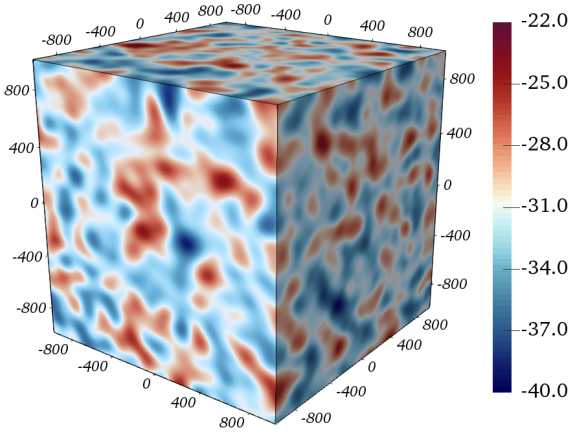

Figure 2. Example of a three-dimensional lnκ field from Sequential Gaussian Simulation (SGS) with isotropic covariance function using Var(lnκ) = 5.3. The permeability (κ) field and thus hydraulic diffusivity fields are readily obtained from the lnκ field.

used in each domain type, and our treatment of fluid flow in the fracture network of the DFNM domain. In Section 2.3, we describe the approach used to estimate the effective hydraulic diffusivity based on pressure diffusion and in Section 2.4, we describe the approach used to estimate the seismic diffusivity from r-t plot analysis.

2.1 SGS Domains

There is a long history of previous work on flow and transport in heterogeneous porous media based on numerical simulations in computer-generated spatially correlated random fields (Deutsch & Journel, 1998; Tompson et al., 1989). To generate such a field for hydraulic diffusivity, we first generate a logarithm of permeability field (lnκ, where κ has units of m^2) with an isotropic, Gaussian covariance function using the GeoStat-Framework (i.e. GSTools module in Python) (Müller & Schüler, 2020). We simulate ten realizations of the SGS domain at four different values of the variance of lnκ (Var(lnκ) = 0.53, 1.325, 2.65 and 5.3), for a total of 40 SGS domain realizations. Note that a value of zero for Var(lnκ) entails a perfectly homogeneous domain.

The SGS domains are discretized using a structured, tetrahedral mesh with vertices uniformly spaced at 20 meters apart. The autocorrelation length of the SGS covariance function is 100 meters (five times larger than the grid spacing of the numerical mesh) and the sides of the cubic domain are two kilometers (20 times larger than the autocorrelation length). An example of the resulting lnκ field is shown in Figure 2. A correlated, random field of permeability (κ) for use in equations (1) or (2) is readily obtained by taking the exponential of the lnκ field.

After generating the field of permeability, the correlated, random field of hydraulic diffusivity is found using the well established definition of hydraulic diffusivity given in

Table 2. Summary of parameters for SGS domains.

Parameter	Description	Value or Range	Unit
E($\ln\kappa$)	mean value of $\ln\kappa$	-31.0	–
Var($\ln\kappa$)	variance of $\ln\kappa$	0.53 - 5.3	–
ϕ	porosity	0.05	–
β_m	compressibility of porous medium	$7.0 \cdot 10^{-11}$	Pa^{-1}
$D_{h,SGS}$	local hydraulic diffusivity	$5.2 \cdot 10^{-5}$ - $3.4 \cdot 10^{3}$	$\mathrm{m/s}^2$

equation (2). When evaluating this expression, we have assumed typical, constant values for μ ($8.9 \cdot 10^{-4}$ Pa $\cdot$ s), ϕ (0.05), β_f ($4.4 \cdot 10^{-10}$ Pa^{-1}), and β_m ($7.0 \cdot 10^{-11}$ Pa^{-1}) that are reflective of a highly fractured, low permeability rock in which IIS most often occurs (Bear, 1972; Charbeneau, 2006; De Marsily, 1986; Freeze & Cherry, 1987). Note that permeability can vary spatially by several orders of magnitude within a heterogeneous domain, whereas porosity varies within a relatively narrow range in a given formation (Gelhar, 1993). Therefore, using a spatially variable permeability along with a uniform porosity is an acceptable approximation that is common in studies of fluid flow in heterogeneous porous media. The field of spatially variable permeability along with uniform values of all other parameters in equation (2) produces a random, spatially correlated field of hydraulic diffusivity, as desired. A summary of the model parameters specific to the SGS domains are given in Table 2. As mentioned previously, the weak points are seeded throughout the SGS domains and assigned a hypothetical fracture orientation. The final set of weak points for the SGS domains is shown in Figure 3, colored based on the weak point triggering pressure increment (p_t^{wp}).

2.2 DFNM Domains

In a domain of highly fractured, low permeability rock, the fracture network represents a well-connected pathway of relatively high hydraulic diffusivity through which pressure increments can propagate rapidly. Since most cases of IIS occur in fractured rock, it is critical to consider models of subsurface heterogeneity that explicitly represent these connected fracture networks. In the following sections, we describe the methodology specifically employed for the fractured rock domain.

2.2.1 Fracture Network and Numerical Mesh Generation

The DFNM domain is fully three-dimensional, with the fracture network represented by penny-shaped fractures of finite thickness embedded within the rock matrix. This methodology has been previous presented (Birdsell et al., 2018; Haagenson et al., 2018; Haagenson & Rajaram, 2020) and is also referred to as an upscaled discrete fracture matrix model (UDFM) by Sweeney et al. (2020). The primary benefits of this approach, as opposed to modeling the fracture network alone, is that we can directly account for fluid flow in

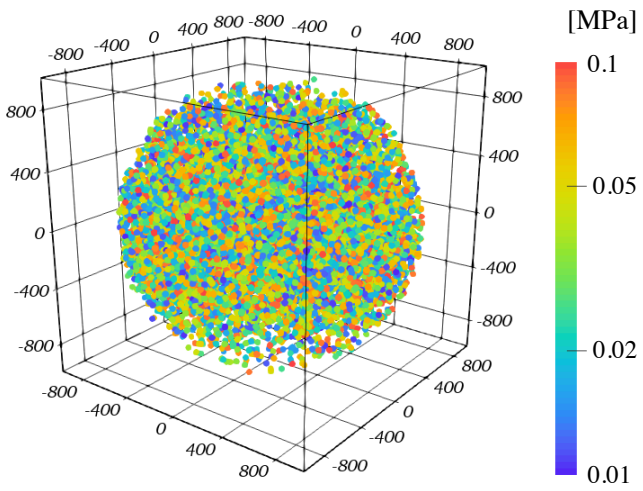

Figure 3. The locations of the weak points for the SGS domains colored by their respective triggering pressure increment p_t^{wp}. Note that weak points are randomly distributed within one kilometer of the injection location and have triggering pressure increment values limited to the range of 0.01 and 0.1 MPa.

the rock matrix (including leak-off from the fracture network) while keeping the mathematical and numerical formulations relatively simple.

The discrete fracture network (DFN) is initially generated as a three-dimensional network of two-dimensional fractures using dfnWorks – a fracture network generator and flow solver developed at Los Alamos National Laboratory (J. D. Hyman et al., 2015). The DFN is generated using a truncated power law distribution for fracture radius (ranging between 200 and 400 meters) and a uniform distribution for fracture orientation. The fracture apertures (b) are linearly related to the fracture radii and range between 0.2 and 0.5 millimeters. The DFN used in this study was chosen for illustrative purposes, and the approach can readily be extended to include alternative fracture network characteristics (such as fracture families with preferred orientations). The three-dimensional DFN used in this study is presented in Figure 4(a).

To build the final three-dimensional mesh, the DFN is overlaid onto a structured tetrahedral mesh. Mesh cells overlapped by a fracture are then recursively refined using an octree-based mesh refinement method (Sweeney et al., 2020). The number of refinement steps is stipulated, with more steps leading to finer mesh resolution near the mesh elements that represent the DFN. This process is depicted in Figure 4(b). The final result is a three-dimensional tetrahedral mesh containing cells to represent the fractures and the rock matrix separately. The octree-based mesh refinement method produces a DFNM domain that accurately reflects the topology of the original DFN, although with "staircase" shaped fractures as a secondary feature. A portion of the full mesh is

Table 3. Summary of parameters for DFNM domain.

Parameter	Description	Value or Range	Unit
κ	permeability of rock matrix	10^{-17}	m^2
ϕ	porosity of rock matrix	0.05	–
β_m	compressibility of rock matrix	$2.0 \cdot 10^{-10}$	Pa^{-1}
$D_{h,m}$	hydraulic diffusivity of rock matrix	$5.0 \cdot 10^{-5}$	m^2/s
b	fracture aperture	0.2-0.5	mm
K_n	normal stiffness of fractures	$3.0 \cdot 10^{-11}$	Pa/m
$D_{h,frac}$	hydraulic diffusivity of fractures	$2.2 \cdot 10^2 - 3.3 \cdot 10^3$	m^2/s

shown in Figure 4(c) and the final DFN after the octree-based mesh refinement method in Figure 4(d). For the DFNM domain in this study, the initial structured mesh is a cube with side lengths of two kilometers and vertices spaced uniformly at 100 meters apart. There are four iterations of octree-based mesh refinement around the fracture cells, leading to a final model fracture cell width of 6.25 meters (which we refer to as b_p) and a high degree of mesh refinement around the fracture network. Clearly, in a field-scale model, fracture cell widths cannot be refined down to the true fracture aperture (i.e. b), which is typically in the sub-millimeter range. Interface finite element formulations can handle narrow fractures treated as discontinuities (Abushaikha et al., 2015; Berre et al., 2019; Fumagalli & Scotti, 2013; Geiger et al., 2010; Odsæter et al., 2019); however, these approaches typically require highly specialized numerical methods beyond the current capabilities of most general-purpose FEM software (e.g. FEniCS) and limit the domain to either two dimensions or simple DFN geometries in three dimensions (Sweeney et al., 2020). Alternatively, a practically reasonable model fracture width (b_p) that is much larger than the true fracture aperture (b) may be used, so long as the model representation of the fracture is hydraulically equivalent to the true fracture and leak-off fluxes from the fracture to the adjacent rock matrix are calculated accurately. Such an approach has been employed in previous work (Birdsell et al., 2015, 2018; Bower & Zyvoloski, 1997; Chaudhuri et al., 2013; Pandey & Rajaram, 2016; Pandey et al., 2017; Sweeney et al., 2020). In Section 2.2.2, we further discuss the hydraulic equivalence between the model representation of fractures and the true fracture. A summary of the model parameters specific to the DFNM domain is presented in Table 3.

The zones of relatively high hydraulic diffusivity in the SGS realizations with $\mathrm{Var}(\ln\kappa) = 5.3$ (i.e. the largest variance considered) have hydraulic diffusivity values comparable to those found in the fractures of the DFNM domain. The major difference between the domains is that zones of high hydraulic diffusivity are well-connected in the DFNM domain. To illustrate this, we plot the distribution of hydraulic diffusivity within the fracture network of the DFNM domain in Figure 5(b), and compare it with the locations of equivalently high hydraulic diffusivity in an example of the SGS domains (with $\mathrm{Var}(\ln\kappa) =$

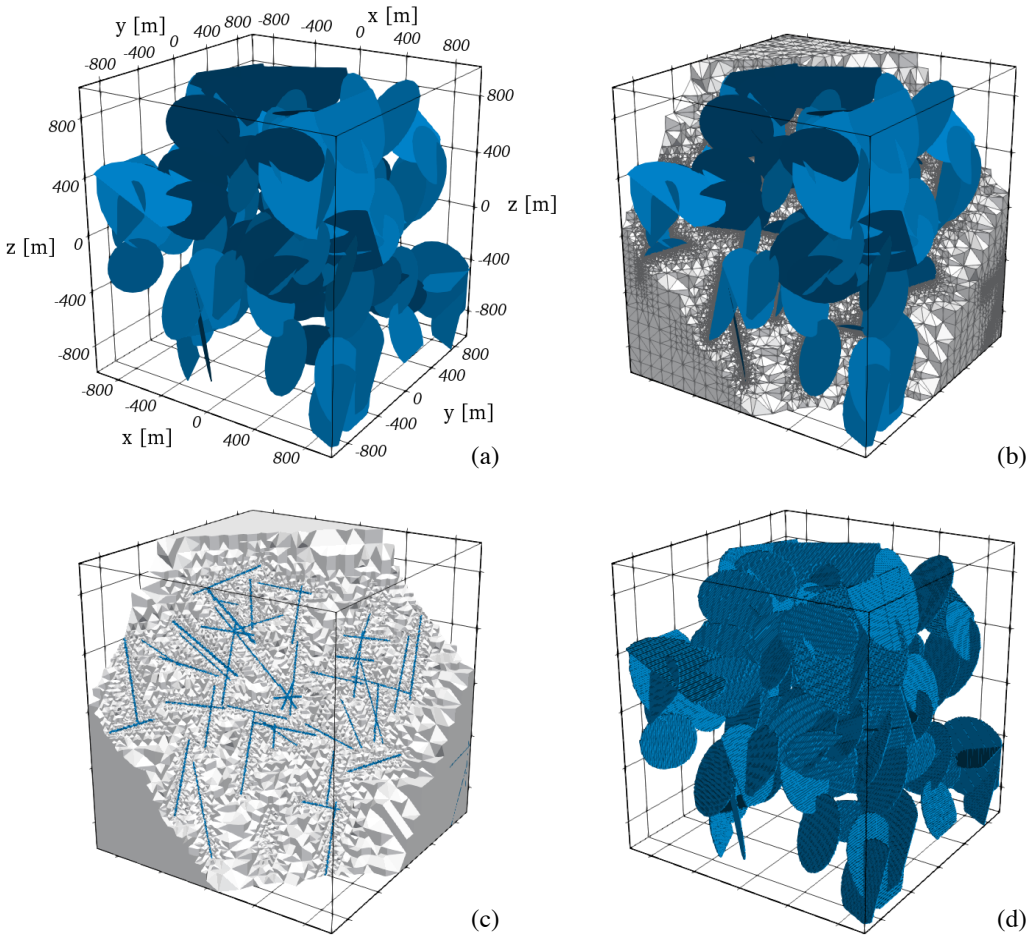

Figure 4. A visualization of how the DFNM numerical mesh is generated. The matrix cells are shown in white and the fracture cells are shown in blue. (a) The initial DFN of two-dimensional fractures generated using dfnWorks. (b) The original DFN overlaid onto the final three-dimensional, tetrahedral mesh. The cell edges are highlighted in dark grey to clearly visualize the high degree of mesh refinement near the fracture cells. (c) A portion of the final three-dimensional mesh, showing locations of the fracture cells within numerical mesh. (d) The final DFN of the three-dimensional mesh.

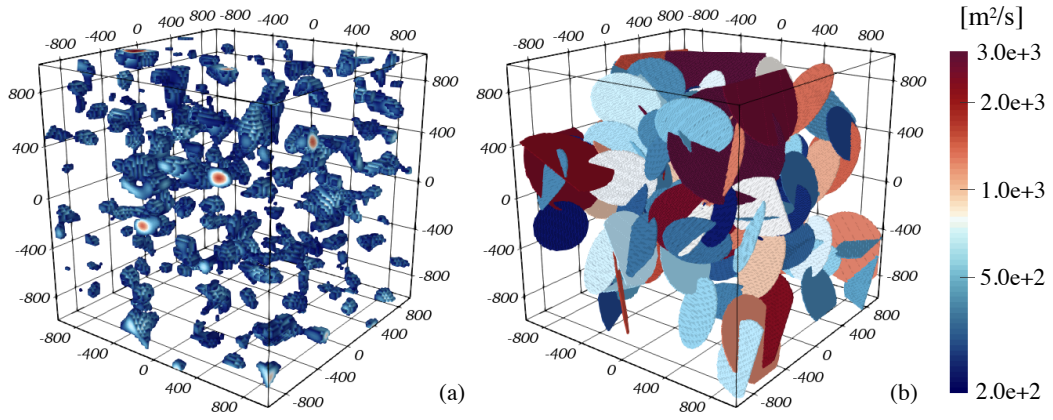

Figure 5. A visual comparison of the spatial distribution of the upper range of hydraulic diffusivity values (i.e. values of hydraulic diffusivity found in the DFN) for (a) the SGS domain and (b) the DFNM domain. Note that relatively high hydraulic diffusivity values are exclusively found in the fracture network for the DFNM case, which creates well-connected pathways throughout domain.

5.3) in Figure 5(a). Notice that zones of relatively high hydraulic diffusivity are not well-connected in the SGS case, whereas they are in the DFNM domain. We expect that the enhanced connectivity in the DFNM domain will cause pressure increments to diffuse rapidly within the fracture network, leading to more rapid propagation of seismicity compared to the SGS domains.

2.2.2 Flow and Seismicity in a Fracture Network

Fluid flow in the rock matrix portion of the DFNM domain is governed by equation (1). Here, we discuss the treatment of equation (3) for modeling fluid flow in the fracture network. The DFNM domain contains both the fracture network and rock matrix (as discussed in Section 2.2.1), allowing us to drop L_m from equation (3) as leak-off from the fracture network is automatically considered by allowing fluxes across fracture-matrix interfaces. The storage term in equation (3) may be expanded following the approach of Rutqvist et al. (1998), giving

$$\rho_f \left(\beta_f b + 1/K_n\right) \frac{\partial p}{\partial t} - \nabla \cdot \left(\frac{\rho_f b^3}{12\mu} \nabla p \right) = Q_f \tag{7}$$

where K_n is the normal stiffness of the fracture, which can be measured using laboratory experiments (Bandis et al., 1983). Following the approach of Chaudhuri et al. (2013) and others (Birdsell et al., 2015, 2018; Bower & Zyvoloski, 1997; Pandey & Rajaram, 2016; Pandey et al., 2017), we define the permeability of the fractures as

$$\kappa_{frac} = \frac{b^3}{12 b_p}. \tag{8}$$

Typically, fracture permeability is given by the well-known expression $\kappa_{frac} = b^2/12$; however, scaling this expression with b/b_p in equation (8) accurately accounts for the discrepancy between b and b_p. This approach in fact rigorously ensures that the model fractures are hydraulically equivalent to the actual fractures (i.e. the total flow rate and rate of pressure diffusion through the model fracture are identical to those in the actual fractures) (Birdsell et al., 2015, 2018; Bower & Zyvoloski, 1997; Chaudhuri et al., 2013; Pandey & Rajaram, 2016; Pandey et al., 2017). Substituting equation (8) into equation (7) and rearranging gives

$$\frac{1}{b_p}\left(\beta_f b + 1/K_n\right)\frac{\partial p}{\partial t} - \nabla \cdot \left(\frac{\kappa_{frac}}{\mu}\nabla p\right) = Q_v. \tag{9}$$

This is the final form of the governing equation for pressure diffusion in the fracture cells of the DFNM domain. In equation (9), we have divided through by b_p and dropped ρ_f from the first two terms assuming it is a constant value. Notice that Q_f has converted to Q_v, the source or sink term of fluid volume per unit volume of the fracture. Similar to equation (1), we assume that the parameters (i.e. fracture aperture, normal fracture compressibility, fracture permeability, and fluid viscosity) in equation (9) are independent of fluid pressure leading to a linear diffusion equation. Some fracture parameters (particularly fracture aperture) are known to be pressure and stress dependent (e.g. normal dilation (Bandis et al., 1983) or shear dilation (Rong et al., 2016; Ye & Ghassemi, 2018)), which may influence the behavior of fluid flow and propagation of seismicity in the DFNM domain. Since the main objective here is to investigate the influence of heterogeneity, we use a linear form of equation (9). We intend to investigate the nuanced influence of nonlinear fluid flow in fracture networks on the behavior of seismicity in future work. From equations (8) and (9), we see that the hydraulic diffusivity of the fractures can be readily defined as

$$D_{frac} = \frac{b^3}{12\mu\left(\beta_f b + 1/K_n\right)}. \tag{10}$$

Contrary to the simulations of the SGS domains, weak points for the DFNM domain are exclusively seeded within the fracture cells, as seismic events are expected to be triggered by the failure of a fracture and not within the intact rock matrix. This approach allows us to investigate the effect of fracture orientation on the spatiotemporal patterns of seismicity in the DFNM case. Using the strike and dip angles and randomly generated coefficients of friction (ranging between 0.6 and 0.7), we calculate the fluid pressure increment at which each weak point would fail (p_t^{wp}) according to the well-known Mohr-Coulomb failure criterion given in equation (4). The locations of the weak points for the DFNM domain are shown in Figure 6, colored according to the weak point triggering pressure increment values. Note that for some fracture orientations, any trigger-

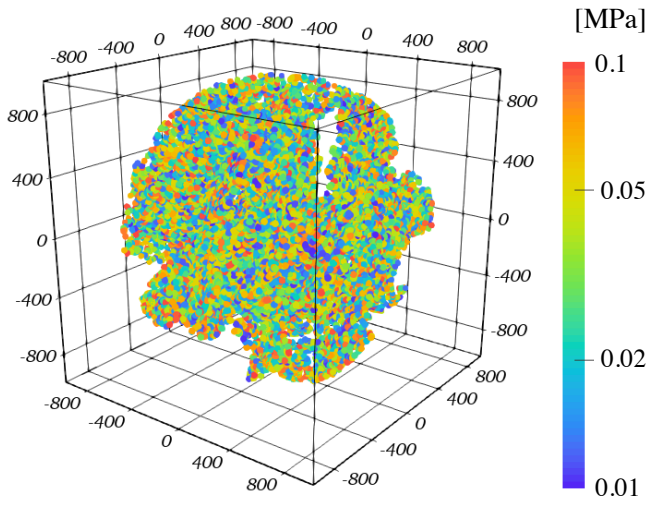

Figure 6. The locations of the weak points colored by their respective triggering pressure p_t^{wp} (in the range of 0.01 to 0.1 MPa) for the DFNM domain. Note that the weak points are randomly distributed in DFN alone, within one kilometer of the injection location. Weak point triggering pressure increment values are based on the orientation of given fracture. Note that some fractures have orientations that inhibit the potential for seismicity and thus do not contain any weak points.

ing pressure increment would fall outside the assumed range for triggering pressure increments associated with IIS (i.e. 0.01 to 0.1 MPa). Therefore, weak points are not assigned within these fractures. Still, these fractures provide pathways of relatively high diffusivity for pressure increments to diffuse along – eventually reaching a fracture more prone to failure.

2.3 Estimating Effective Hydraulic Properties of Heterogeneous Domains

The effective hydraulic diffusivity of the heterogeneous domains were found using the well established concept of effective permeability (Chrysikopoulos, 1995; Dagan, 1979, 1989; Dykaar & Kitanidis, 1992a, 1992b; Gelhar, 1993; Gutjahr et al., 1978; Paleologos et al., 1996; Zhang, 2001). The effective permeability of each heterogeneous domain (κ_{eff}) was rigorously estimated using a numerical permeameter test in each axial direction (Fernàndez-Garcia et al., 2005). Constant pressure boundary conditions were applied to opposite sides of the domain with all other boundaries made impervious, generating fluid flow from the high pressure to low pressure boundary. The effective hydraulic permeability in the i^{th} direction is estimated with the total fluid flow through the domain Q_i at steady state conditions using

$$\kappa_i = \frac{Q_i \mu L}{A \Delta p} \tag{11}$$

where L is the length of the domain in the i^{th} direction, A is the cross-sectional area of the domain perpendicular to the i^{th} direction, and Δp is the difference between the pressures at the inflow and outflow boundaries. The numerical permeameter test aligns well with the conventional definition of the effective permeability: the permeability of a homogenous domain that produces an equivalent flow to the ensemble mean of the heterogeneous domain under steady flow conditions (Chrysikopoulos, 1995; Dagan, 1989; Dykaar & Kitanidis, 1992a, 1992b; Gelhar, 1993; Paleologos et al., 1996; Sanchez-Vila et al., 2006; Zhang, 2001).

Note that evaluating equation 11 for an estimate of the effective permeability requires an accurate and mass conserving solution of the flow field, such that Q_i is well constrained. Therefore, we employ a mixed finite element method (MFEM) to solve Darcy's law and a general form of fluid continuity simultaneously in the numerical permeameter test (Brezzi et al., 1985; Brezzi & Fortin, 2012; Traverso et al., 2013; Younes et al., 2010).

Given the isotropic covariance function of the SGS domains and the high fracture density and random fracture orientations in the DFNM domain, both domain types are expected to be hydraulically isotropic at large scales. After conducting the numerical permeameter test in each axial direction, we found the effective permeabilities in the three directions varied by less than 7%, which is consistent with the expectation of isotropy. We therefore estimate the effective permeability of the heterogeneous domains as the average of the permeabilities in the three axial directions (i.e. $\kappa_{eff} = (\kappa_{xx}+\kappa_{yy}+\kappa_{zz})/3$).

The effective hydraulic diffusivity (D_{eff}) of each SGS domain was then calculated using equation (2), with the effective permeability value (κ_{eff}) from the numerical permeameter test and the uniformly applied values of all other parameters. To confirm that this estimated value of the effective hydraulic diffusivity accurately describes the macroscale behavior of the mean pressure field within the SGS domain during fluid injection, we compared the directionally averaged pressure increment (denoted as p_{avg} and is found by averaging the pressure increment over the surface of a sphere with a given radius centered at the injection location) to the pressure increment predicted by the well-known solution to the three-dimensional, linear diffusion equation. This solution (which describes the evolution of pressure increment in response to a point source of fluid in a homogeneous and isotropic porous medium) is written as

$$p(r,t) = \frac{Q\mu}{4\pi\kappa r}\text{erfc}\left(\frac{r}{\sqrt{4Dt}}\right) \tag{12}$$

where erfc is the complementary error function (Carslaw & Jaeger, 1959). The comparison is shown in Figure 7(a) at three separate times during the numerical simulation for an example of the SGS domains (where $\text{Var}(\ln\kappa) = 5.3$). Generally, the plot shows a good agreement between the predicted profile and the directionally averaged profile at radial distances beyond 200 meters (which is twice the correlation length of the SGS covariance function). Closer to the injection location, the behavior of pressure diffusion is

controlled by the local permeability in the vicinity of the fluid source in any individual SGS realization (as permeability does not vary significantly within 200 meters, which is only twice the correlation length). At radial distances of approximately two correlation lengths or more, however, pressure diffusion appears to be controlled by the effective permeability measured by the numerical permeameter test. This is expected, as pressure diffusion at this radial distance is sampling a larger volume of the SGS domain, which will capture the full range of diffusivity values from the correlated, random field (Guadagnini et al., 2003; Naff, 1991). At the three times considered, normalized-root-mean-square-error ranges between 0.05 and 0.10 while the Nash-Sutcliffe model efficiency coefficient ranges between 0.82 and 0.97. This shows a good fit between the directionally averaged pressure profile and equation (12) using D_{eff} of the SGS domain, which indicates that the effective hydraulic diffusivity estimated for the SGS domains accurately describes the average, macro-scale behavior of pressure diffusion during fluid injection.

For the DFNM domain, the material porosity and compressibility vary dramatically, with widely disparate values between the rock matrix and the fractures. Thus, is it not possible to evaluate equation (2) directly as in the SGS domains. Instead, the effective hydraulic diffusivity (D_{eff}) of the $DFNM$ domain was estimated using a numerical simulation of fluid injection. We simulated pressure diffusion in response to a point source of fluid injection and found the profile of directionally averaged pressure increment (p_{avg}) at various times during the simulation. Next, the effective hydraulic diffusivity of the DFNM domain was estimated by fitting equation (12) to the directionally averaged profile using a least squares nonlinear regression method. Results of this fitting process are shown in Figure 7(b). At the three times considered, normalized-root-mean-square-error ranges between 0.04 and 0.09 while the Nash-Sutcliffe model efficiency coefficient ranges between 0.77 and 0.95.

2.4 Estimating Seismic Diffusivity

Most approaches to r-t plot analysis are based on tracking the diffusive propagation of the triggering front (Delepine et al., 2004; Shapiro et al., 1997; Shapiro & Müller, 1999; Shapiro et al., 2002; Shapiro, 2015). Researchers estimate a diffusivity (which we call seismic diffusivity following the terminology of Talwani and Acree (1985)) by fitting expressions for the location of the triggering front to the upper envelope of the seismic data cluster found in r-t plots (which is the approximate location of the hypothetical triggering front). For example, Shapiro et al. (1997) proposed the expression $r_t = \sqrt{4\pi Dt}$ for tracking the location of the triggering front (r_t) in time, where D is the diffusivity value being estimated. This expression is widely used for analyzing the spatiotemporal patterns of seismicity from r-t plots and for producing estimates of seismic diffusivity (Antonioli et al., 2005; Chen et al., 2012; Goebel et al., 2017; Goertz-Allmann et al., 2017; Haffener et al., 2018; Hummel & Shapiro, 2012; Ingebritsen & Manning, 2010; Shapiro & Dinske, 2009a; Yong et al., 2018; Yu et al., 2019). Note that this approach is based on interpreting the propagation of fluid pressure increments as a wave problem (Shapiro,

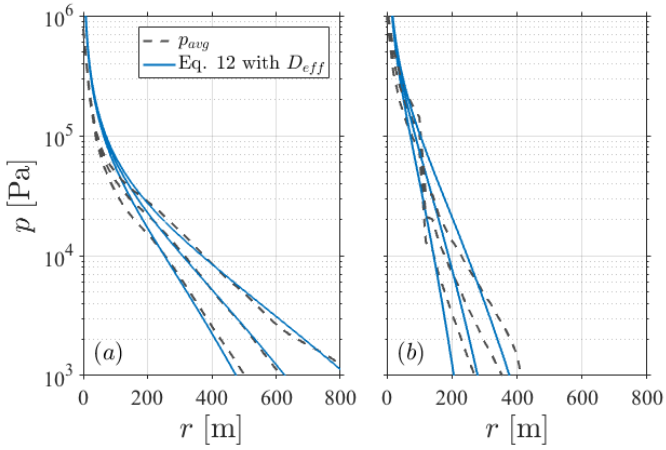

Figure 7. Plots of directionally averaged pressure increment (p_{avg}) from fluid injection simulations overlaid with equation (12) using the effective hydraulic diffusivity (D_{eff}). (a) Results from a SGS realization, providing evaluation of the fit of equation (12) using D_{eff} at three different times: 0.5, 1.0, and 2.0 days. For the SGS domains, D_{eff} stems from equation (2) with κ_{eff} from the numerical permeameter simulation and the uniformly applied parameters to all SGS domains. At the three times considered, normalized-root-mean-square-errors are 0.10, 0.07, and 0.05 and Nash-Sutcliffe model efficiency coefficients are 0.82, 0.92, and 0.97 respectively. (b) The DFNM domain results, where equation (12) is fit with nonlinear regression (using κ_{eff} from the numerical permeameter simulation) at three different times (0.125, 0.25, and 0.5 days) in order to obtain an estimate of D_{eff}. At the three times considered, normalized-root-mean-square-errors are 0.09, 0.06, and 0.04 and Nash-Sutcliffe model efficiency coefficients are 0.77, 0.89, and 0.95 respectively.

2015), rather than as a diffusion of pressure increments in a three-dimensional porous media.

Here, we propose using linear diffusion (based on well established theory of fluid flow in porous media) to track the location of the isobaric surface with pressure increment value equal to p_t, which is synonymous with the triggering front (Bear, 1972; Charbeneau, 2006; Cleary, 1977; De Marsily, 1986; Rice & Cleary, 1976; Rudnicki, 1986; Verruijt, 2013). The main benefit of this approach (as opposed to the one proposed by Shapiro et al. (1997)) is that incorporates physically important parameters, such as the injection rate and the threshold triggering pressure increment (Haagenson & Rajaram, 2020). These parameters are expected to influence the propagation of the triggering front through the subsurface and should thus be incorporated. By rearranging equation (12), the arrival time of the triggering front (t_t) at any given radial distance from the injection location in an infinite, homogeneous, and isotropic porous medium can be written as

$$t_t(r) = \frac{r^2}{4D_s}\text{erfc}^{-1}\left(\frac{4\pi k p_t r}{Q\mu}\right)^{-2} \tag{13}$$

where D_s is the seismic diffusivity associated with the diffusive propagation of the triggering front and erfc^{-1} is the inverse of the complementary error function (Carslaw & Jaeger, 1959). Note that equation (13) does not provide an explicit equation for the radius of the triggering front as a function of time. Nonetheless, it can still be fit to the upper envelope of the seismic data cluster found in r-t plots in order to produce an estimate of the seismic diffusivity. It is clear from equation (13) that the seismic diffusivity can in fact be interpreted as the hydraulic diffusivity of a hypothetical, homogeneous domain that (when subjected to the same injection conditions) approximately produces the same propagation of the triggering front as observed in the r-t plot based on seismic data from the real-world, heterogeneous domain. This interpretation agrees well with the concept of seismic diffusivity presented by Talwani and Acree (1985) and with the methods of Shapiro et al. (1997) and Shapiro (2015).

3 Results of Pressure Diffusion and Induced Seismicity

The results from the numerical simulations of both the SGS and DFNM domains are presented in the following two sections. We present results of both pressure diffusion and induced seismicity in three-dimensional domains, which illustrates the general influence of heterogeneity. We also examine the behavior of the simulated IIS in r-t plots, which provides insights into the concept of seismic diffusivity and its potential distinction from the effective hydraulic diffusivity of the heterogeneous domains.

3.1 SGS Domain Results

We begin by investigating the influence of heterogeneity on the patterns of IIS in the context of SGS domains, to gain a fundamental understanding of the influence of heterogeneity on the spatiotemporal patterns of IIS in relatively simple representations of

subsurface heterogeneity. As already mentioned, we performed fluid injection simulations in 40 different realizations of the SGS domain, with ten realizations at each value of Var($\ln\kappa$) considered (i.e. 0.53, 1.325, 2.65, 5.3). Figure 8 shows the pressure solution from one example realization of the SGS domain at each value of Var($\ln\kappa$) to illustrate the three-dimensional patterns of pressure diffusion. Cutaway sections show the internal distribution of fluid pressure. Portions of the domain with pressure increment below the threshold triggering pressure increment (p_t) are not shown. In essence, the outer, dark blue contour (which represents a pressure increment value of p_t) shows the location of the triggering front in three-dimensional space, revealing the clear influence of heterogeneity. Figure 8 shows that as the value of Var($\ln\kappa$) increases, the pressure contours and thus the triggering front deviate farther from radial symmetry. We see in the Var($\ln\kappa$) = 5.3 case shown in Figure 8(d) (i.e. the largest value of Var($\ln\kappa$) considered) that p_t has propagated much farther in certain directions than others, which correspond to zones of relatively higher hydraulic diffusivity.

Figure 9 shows the r-t plot from one of the SGS domain realizations with Var($\ln\kappa$) = 5.3, overlaid with the maximum radial distance reached by the threshold triggering pressure increment (denoted by $r_{max}(p = p_t)$) and the radial distance at which the directionally averaged pressure increment (i.e. the averaged pressure increment over a sphere of a given radius) equals the threshold triggering pressure increment (denoted by $r(p_{avg} = p_t)$). First, we see clearly that the farthest occurring seismicity at any given time approximately coincides with $r_{max}(p = p_t)$. This is the expected result, since weak points with triggering pressure increments near the threshold value of p_t will trigger soon after the arrival of p_t. Comparing the locations of $r_{max}(p = p_t)$ and $r(p_{avg} = p_t)$, we clearly see that $r_{max}(p = p_t)$ propagates much more rapidly. This is due to the presence of zones of relatively high hydraulic diffusivity that allow pressure increments to diffuse rapidly in certain directions away from the injection location. This rapid propagation of p_t will directly influence $r_{max}(p = p_t)$ while the value of $r(p_{avg} = p_t)$ lags behind (due to its very nature as a directional average, meaning it is influenced by the entire distribution of hydraulic diffusivity and not just the relatively high values).

Figure 10 (left) shows the time evolution of $r_{max}(p = p_t)$ and $r(p_{avg} = p_t)$ for each of the ten realizations of the SGS domain, along with the corresponding ensemble average, for each value of Var($\ln\kappa$). At relatively low values of Var($\ln\kappa$) (which correspond to relatively homogeneous media), there is not a large variation in the behavior among the ten realizations and $r_{max}(p = p_t)$ nearly coincides with $r(p_{avg} = p_t)$. As Var($\ln\kappa$) increases, though, we see a larger variation in the behavior of both $r_{max}(p = p_t)$ and $r(p_{avg} = p_t)$ across the ten realizations; although, there is more variability in the behavior of $r_{max}(p = p_t)$. This is expected, as $r_{max}(p = p_t)$ estimates a maximum radial distance of a certain pressure increment value, whereas $r(p_{avg} = p_t)$ is inherently a directionally averaged variable and is, therefore, less sensitive to rapid propagation of p_t in a particular direction. If p_t propagates rapidly in a certain direction relative to others, that will be directly reflected in $r_{max}(p = p_t)$, but will not heavily influence $r(p_{avg} = p_t)$. Despite the increase in variability across realizations, it is clear that the deviation

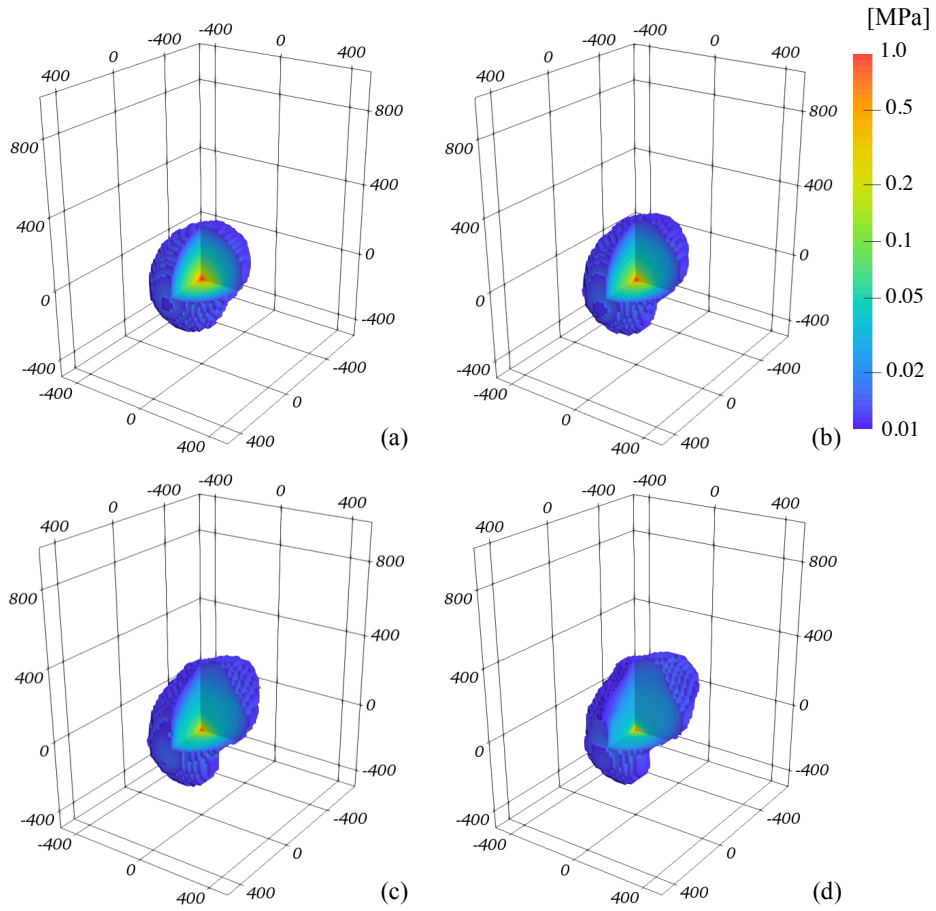

Figure 8. Plots of pressure increment (p) (with cutaway section to show the internal distribution) at the end of the fluid injection simulation (i.e. $t = 12$ hours) for four realizations of SGS domain with the same underlying structure of heterogeneity but scaled to generate varying values of Var($\ln\kappa$): (a) 0.53, (b) 1.325, (c) 2.65, and (d) 5.3. The portions of model domain with pressure increment less than the threshold triggering pressure increment (i.e. $p < p_t$) are not shown.

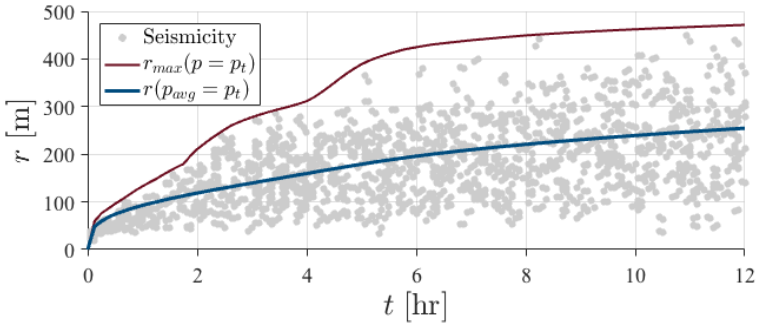

Figure 9. Example r-t plot from an SGS realization with $\mathrm{Var}(\ln\kappa) = 5.3$. The plot is overlaid with the maximum radial distance to which the threshold triggering pressure increment has propagated at any given time (i.e. $r_{max}(p = p_t)$ in red) and the radial distance at which the directionally averaged pressure increment equals the threshold triggering pressure increment (i.e. $r(p_{avg} = p_t)$ in blue).

of $r_{max}(p = p_t)$ from $r(p_{avg} = p_t)$ increases systematically as the degree of heterogeneity increases (i.e. as $\mathrm{Var}(\ln\kappa)$ increases).

From the ten realizations at each value of $\mathrm{Var}(\ln\kappa)$, we also calculated the standard deviations of $r_{max}(p = p_t)$ and $r(p_{avg} = p_t)$, representing their variability across realizations. In Figure 10 (right), we show the ensemble mean of both $r_{max}(p = p_t)$ and $r(p_{avg} = p_t)$ along with two envelopes: one standard deviation above or below the ensemble mean and two standard deviations above or below the ensemble mean. The envelopes around $r(p_{avg} = p_t)$ are much narrower than those around $r_{max}(p = p_t)$, indicating that the propagation of $r_{max}(p = p_t)$ may be more sensitive to the influence of heterogeneity. For the lower values of $\mathrm{Var}(\ln\kappa)$ (i.e. 0.53 and 1.325 where the domains are relatively homogeneous), the envelopes show a significant amount of overlap, indicating that they are not statistically distinct from one another. However, for higher values of $\mathrm{Var}(\ln\kappa)$ (i.e. 2.65 and 5.3 where the domains are relatively heterogeneous), the envelopes do not overlap at late time during the simulations, indicating that $r_{max}(p = p_t)$ and $r(p_{avg} = p_t)$ are statistically distinct from each other, even in the sense of ensemble means.

As commonly done in IIS literature, we use the spatiotemporal patterns of IIS and the propagation of the triggering front to estimate the seismic diffusivity of the heterogeneous domain. The details of our approach are outlined in Section 2.4. To exemplify this approach, we fit equation (13) to the upper envelope of the seismic data cluster (as shown by the dashed red line) in Figure 11(a) using the same example r-t plot found in Figure 9. We see that the triggering front (associated with the seismic diffusivity) generally reflects the approximate behavior of the maximal radial distance to which the threshold triggering pressure increment has propagated (i.e. $r_t \approx r_{max}(p = p_t)$, where r_t is the location of the triggering front according to equation (13)).

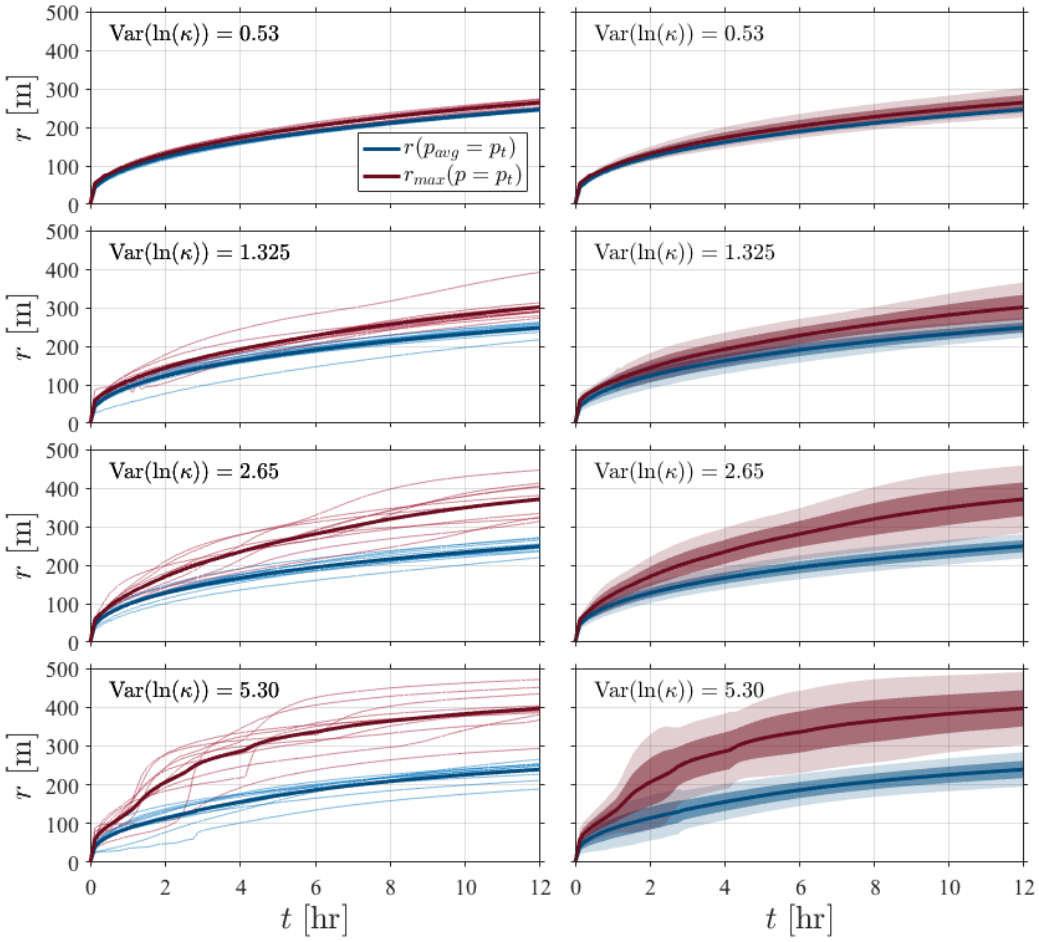

Figure 10. Left: Plots of the radial distance at which the directionally averaged pressure increment equals the threshold triggering pressure increment (i.e $r(p_{avg} = p_t)$) and the maximum radial distance reached by the triggering pressure at any given time (i.e $r_{max}(p = p_t)$). Light blue and red lines show results from each of ten SGS domain realizations. Dark blue and red lines show ensemble mean. Right: Plots of the ensemble of mean $r(p_{avg} = p_t)$ and the ensemble mean of $r_{max}(p = p_t)$. Two envelopes about the ensemble mean are plotted: one standard deviation (dark shading) and two standard deviations (dark shading).

Next, we consider the propagation of the triggering front in a hypothetical homogeneous domain with uniform diffusivity equal to the effective hydraulic diffusivity of the SGS domain, which is overlaid in Figure 11(a) as a dashed blue line. We clearly see that this would drastically underestimate the actual location of the triggering front, the maximal radial distance to which p_t propagates, and the farthest reaches of seismicity at any given time. In fact, equation (13) with the effective hydraulic diffusivity closely coincides with $r(p_{avg} = p_t)$. This is consistent with the concept of the effective hydraulic diffusivity, as it is associated with the evolution of the propagation of directionally averaged pressure contours of any pressure increment value (including the contour of p_t).

We estimate the seismic diffusivity of each SGS domain, and plot these values against $\mathrm{Var}(\ln\kappa)$ in Figure 11(b). Clearly, the seismic diffusivity of the domain increases with $\mathrm{Var}(\ln\kappa)$. This indicates that the rate at which seismicity propagates will also increase with $\mathrm{Var}(\ln\kappa)$. However, we expect the effective hydraulic diffusivity of the SGS domains to increase with $\mathrm{Var}(\ln\kappa)$ as well. We therefore compare the ratio of D_s/D_{eff} for the SGS domains, shown in Figure 11(c). It is clear that, while the variability of this ratio across the SGS realizations increases with $\mathrm{Var}(\ln\kappa)$, the ensemble average of this ratio systematically increases with $\mathrm{Var}(\ln\kappa)$ as well.

For any value of $\mathrm{Var}(\ln\kappa)$, there are some realizations in which the regions of relatively high hydraulic diffusivity are not well-connected. In such realizations, the ratio D_s/D_{eff} will be only slightly above one, as pathways of high hydraulic diffusivity through which pressure increments can rapidly propagate are limited. However, in realizations where regions of relatively high hydraulic diffusivity are well-connected, the ratio D_s/D_{eff} can be quite large and increasing with $\mathrm{Var}(\ln\kappa)$. Overall, the ensemble average captures the average behavior across all realizations and shows a systematic increase of the ratio D_s/D_{eff} with $\mathrm{Var}(\ln\kappa)$.

3.2 DFNM Domain Results

Next, we consider a DFNM domain, which is a better representation of fractured rock formations in which IIS commonly occurs. In the study of SGS domains, we mainly focused on showing that the seismic diffusivity (which is associated with the propagation of $r_{max}(p = p_t)$) and the effective hydraulic diffusivity (which is associated with the propagation of $r(p_{avg} = p_t)$) of the highly heterogeneous SGS domains are not equivalent. In the DFNM domain, the zones of relatively high hydraulic diffusivity (i.e. the fractures) are well-connected (see Figure 5). This develops well-connected pathways of high hydraulic diffusivity (which were only occasionally present in the SGS domains) through which the pressure increment from the injection location can rapidly propagate, causing seismicity to spread rapidly as well. Hence, the discrepancy between the seismic diffusivity and the effective hydraulic diffusivity of the DFNM domain may be larger than in the SGS cases. To evaluate this, we calculate the ratio D_s/D_{eff} for the DFNM domain, and compare it to the values found in the study of the SGS domains.

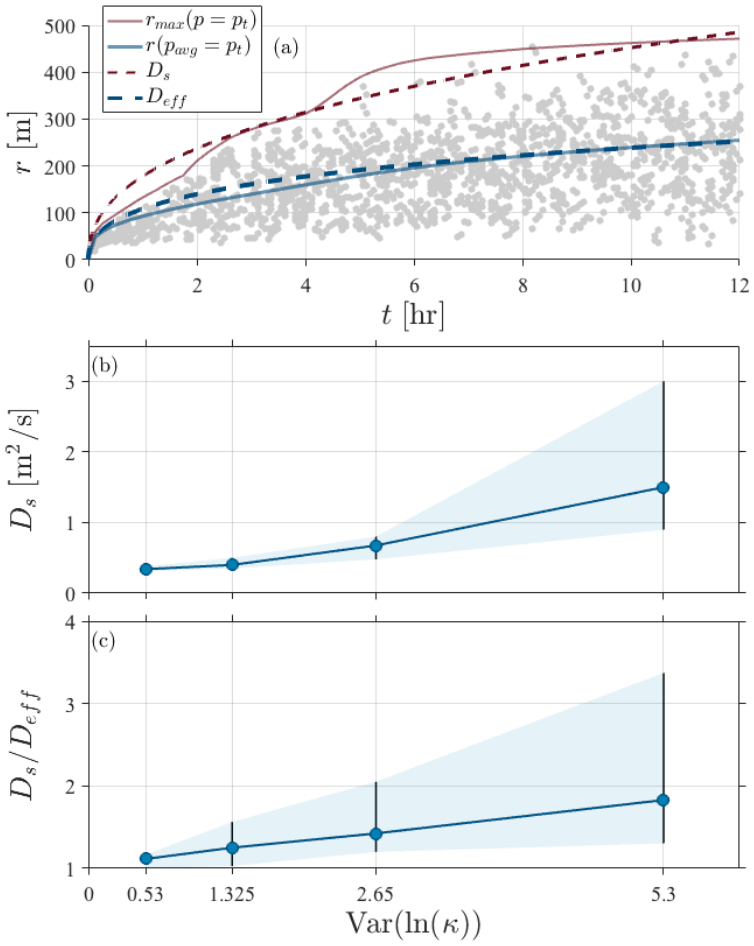

Figure 11. (a) The same r-t plot as shown in Figure 9, with equation (13) overlaid twice: once with D_s (red dashed line) and once with D_{eff} (blue dashed line). (b) Plot of seismic diffusivity at various values of Var(lnκ). Solid blue line is the ensemble mean and shaded region shows range of values from all ten realizations at each value of Var(lnκ). (c) Plot of D_s/D_{eff} at various values of Var(lnκ). Solid blue line is the ensemble mean and the shaded region shows range of values from all ten realizations at each value of Var(lnκ).

Additionally, we highlight one major implication of the discrepancy between the seismic diffusivity and the effective hydraulic diffusivity. If the spatiotemporal patterns of seismicity are not in fact well described by the effective hydraulic diffusivity of a realistic, heterogeneous domain, then the common approach of using homogeneous domains (or layers of homogeneous domains) in numerical simulations of induced seismicity (Brown et al., 2017; Catalli et al., 2016; Dempsey & Riffault, 2019; Keranen et al., 2014; Langenbruch & Zoback, 2016; Langenbruch et al., 2018; Pollyea et al., 2019; Riffault et al., 2018) may be limited. To investigate this, we compare the results of simulated fluid injection in two domains: the DFNM domain and a homogeneous domain with uniform hydraulic diffusivity equal to the effective hydraulic diffusivity of the DFNM domain. As mentioned in Section 2.3, the effective hydraulic diffusivity of the DFNM domain was estimated using numerical permeameter and fluid injection tests and was found to exhibit isotropic behavior. Thus, the equivalent homogeneous domain used here is isotropic as well.

The results of pressure diffusion in response to fluid injection for both domains are shown in Figure 12. It is clear that the threshold triggering pressure increment has propagated to a significantly greater distance away from the injection location in the DFNM case. This is the expected result since fluid flows radially outward in the homogeneous domain, whereas fluid flows primarily in the fracture network of the DFNM domain. Forcing the stipulated injection rate into the relatively small volume of the of the fracture network requires that pressure increments from the injection location propagate more rapidly in the DFNM case than in the homogeneous one. Hence, the threshold triggering pressure increment has propagated to a much farther distance by the end of the injection simulation in the DFNM case.

In Figure 13, we show the locations of induced seismicity triggered during the numerical simulation of fluid injection for each domain. Since the threshold triggering pressure increment propagates much farther in the DFNM case, seismicity in the DFNM case occurs at greater distances away from the injection location as well. Additionally, we see two unique behaviors in the DFNM case. First, events associated with a relatively high triggering pressure increment were triggered much more often in the DFNM case. Since the stipulated fluid injection rate must be accommodated almost entirely by the DFN (which has a relatively small volume), large pressure increments from the injection location must propagate farther into the DFNM domain than in the homogeneous one. This triggers weak points in the simulation of the DFNM domain that are less prone to fail (due to a higher coefficient of friction or an unfavorable fracture orientation that hinders slip). Second, we see in bottom left corner of Fig 13(e) that some fractures of the DFNM domain have actually been pressurized to the threshold triggering pressure increment (p_t) while not experiencing any seismicity. The unfavorable orientation of these fractures limits the potential for seismicity. Still, these fractures act as efficient pathways to facilitate pressure increment propagation. Fluid flow through these fractures may therefore lead to seismicity along a connected fracture that is more favorably oriented for fail-

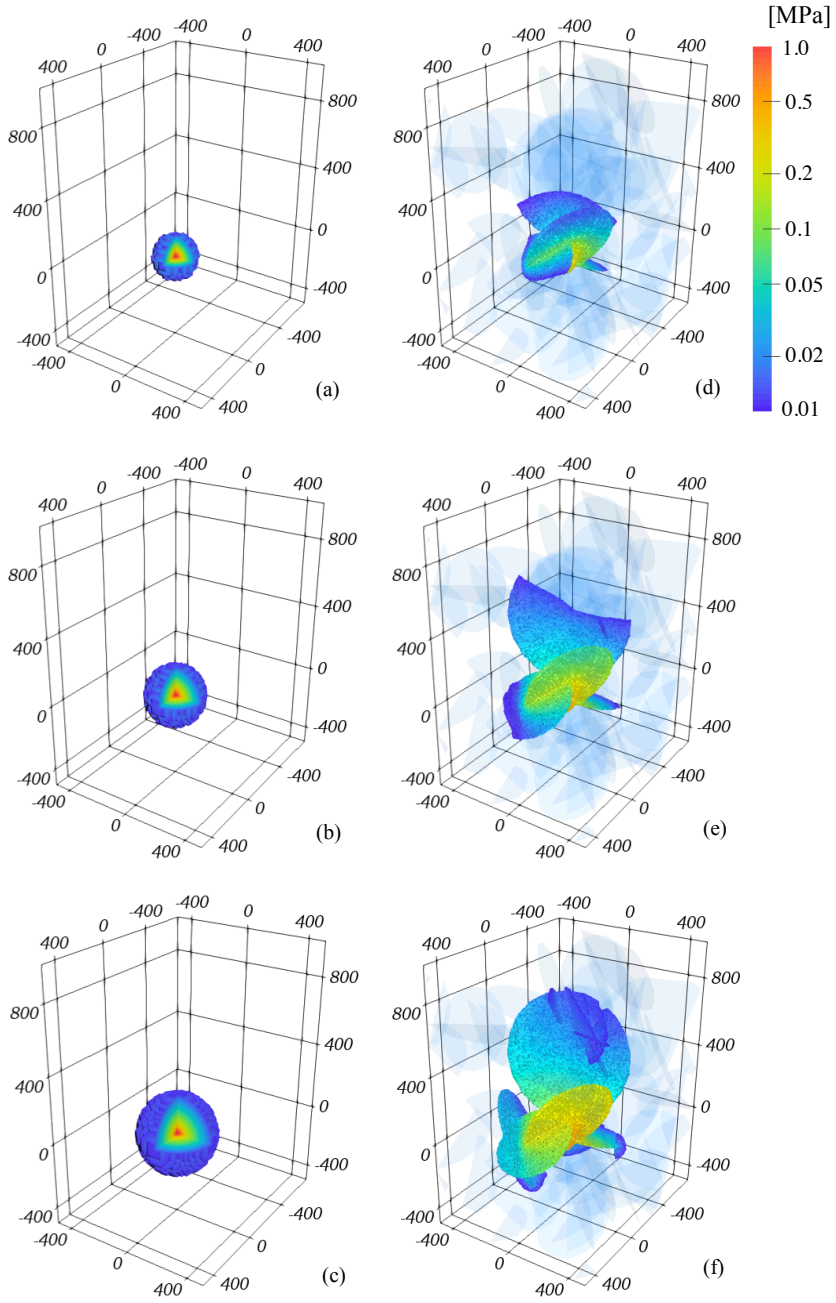

Figure 12. Plots of pressure increment (p) (with cutaway section in (a) - (c) to show the internal distribution) at three different times during the fluid injection simulation ($t = 3$, 6, and 12 hours) for: (a) – (c) the homogeneous domain with uniform hydraulic diffusivity equal to the effective hydraulic diffusivity of the DFNM domain and (d) – (f) the DFNM domain. The portions of model domain with pressure increment less than the threshold triggering pressure increment (i.e. $p < p_t$) are not shown. Fractures of the DFN with pressure increment less than the threshold triggering pressure increment are shaded in transparent blue.

ure, as we see in Figure 13(f). These are examples of the more subtle influences of fracture networks on the behavior of IIS.

If we look at the synthetic dataset of seismicity from both simulations as an r-t plot (shown in Figure 14), we clearly see very different behavior between the equivalent homogeneous and DFNM domains. As expected, seismicity has propagated much farther in the DFNM domain than in the equivalent homogeneous domain. This suggests that equivalent homogeneous domains (which are commonly used in studies of IIS (Brown et al., 2017; Catalli et al., 2016; Dempsey & Riffault, 2019; Keranen et al., 2014; Langenbruch & Zoback, 2016; Langenbruch et al., 2018; Pollyea et al., 2019; Riffault et al., 2018)) may be limited in their ability to replicate the spatiotemporal patterns of IIS as observed in r-t plots from real-world or heterogeneous domains. Next, we examine the behavior of the triggering front in each domain, using equation (13) as described in Section 2.4. As expected, the triggering front in the equivalent homogeneous domain is well described using the effective hydraulic diffusivity. In this case, the triggering front is radially symmetric and thus there should not be any distinction between the seismic diffusivity and the effective hydraulic diffusivity. In the DFNM domain, however, we see that the location of the triggering front is vastly underestimated by equation (13) using the effective hydraulic diffusivity of the domain, as was the case in the highly heterogeneous SGS domains. This again suggests that the seismic diffusivity associated with the diffusive propagation of the triggering front (which was found to be 3.0 m^2/s in the DFNM domain) is larger than the effective hydraulic diffusivity in heterogeneous porous media (which was found to be 0.29 m^2/s in the DFNM domain).

Finally, we consider the ratio of D_s/D_{eff} as we did in the study of SGS domains (see Figure 11(c) for the comparison of this ratio from the SGS domains), which produces a value of 10.2 in the DFNM domain. This shows that in the case of fractured rock, the distinction between the seismic and effective hydraulic diffusivity can be up to one order of magnitude. Moreover, this is considerably larger than the largest ratio found in the SGS cases (i.e. $D_s/D_{eff} = 3.4$), which indicates that the well-connected pathways of the fracture network allow pressure increments to propagate more rapidly in the DFNM domain than in any of the SGS domains considered in this study.

To be thorough, we also performed a simple sensitivity analysis to gain insight into the potential uncertainty associated with the estimate of seismic diffusivity of the DFNM domain. Figure 15 shows the location of the triggering front according to equation (13) using $D_s = 3.0$ m^2/s along with various other values of seismic diffusivity: $0.1D_s$, $0.5D_s$, $2D_s$, and $10D_s$. It is clear from Figure 15 that even relatively small variations in the seismic diffusivity (i.e. $0.5D_s$ and $2D_s$) alter the behavior of the triggering front enough that it no longer fits well to the upper envelope of the seismic data cluster. This suggests that we can be reasonably confident in the values of seismic diffusivity estimated with the triggering front plotted in Figure 14(b).

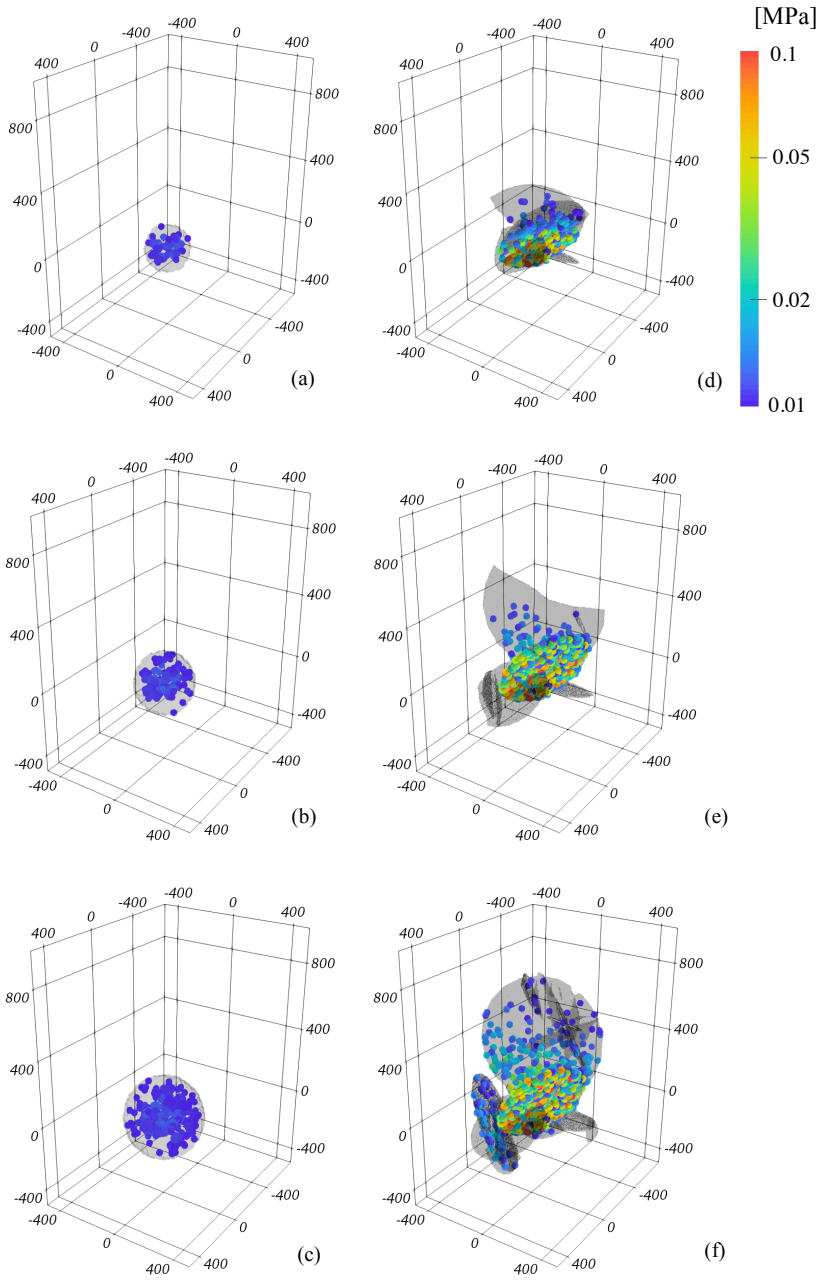

Figure 13. Plots of seismicity during the injection simulation at three different times during the injection simulations (t = 3, 6 and 12 hours) for: (a) - (c) the homogeneous domain with uniform hydraulic diffusivity equal to the effective hydraulic diffusivity of the DFNM domain and (d) - (f) the DFNM domain. The seismic events are colored based the weak point triggering pressure increment (p_t^{wp}). The spatial extent to which threshold triggering pressure increment (p_t) extends (which corresponds to the plotted portions in Figure 12) is shaded in dark grey.

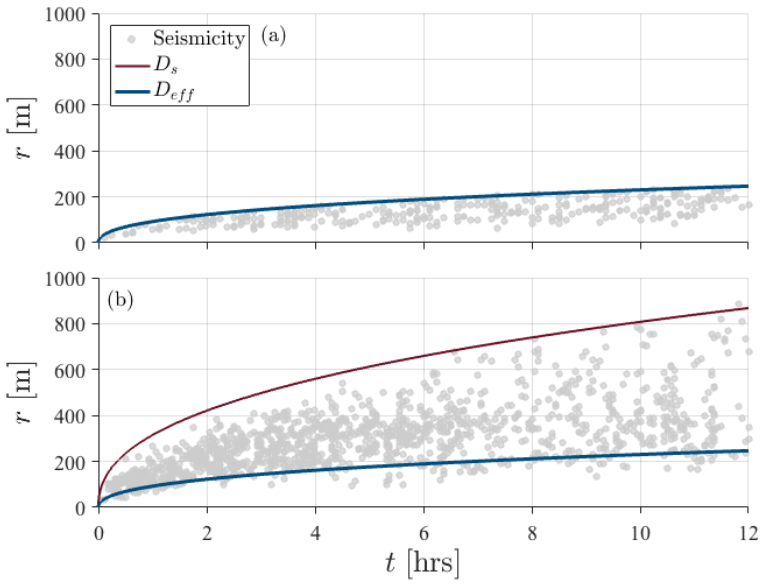

Figure 14. An r-t plot using the synthetic dataset of seismicity from the fluid injection simulation for (a) the homogeneous domain with uniform hydraulic diffusivity equal to the effective hydraulic diffusivity of the DFNM domain and (b) the DFNM domain. Each r-t plot is overlaid with equation (13) using the effective hydraulic diffusivity of the DFNM domain (D_{eff}). Equation (13) is also plotted with the fitted estimate of seismic diffusivity (D_s) of the DFNM domain.

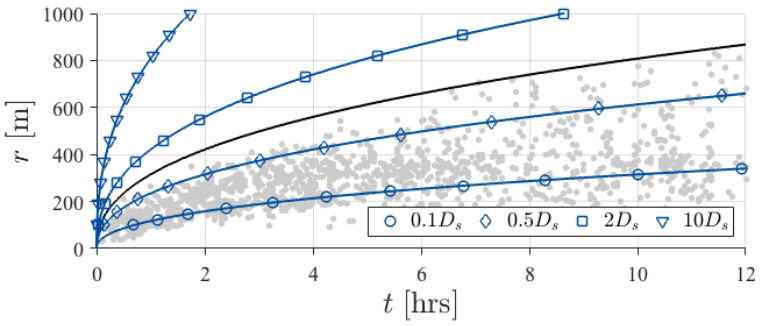

Figure 15. An r-t plot using the synthetic dataset of seismicity from the fluid injection simulation for the DFNM domain, overlaid with equation (13) using the estimated value of seismic diffusivity (D_s) as well as $0.1D_s$, $0.5D_s$, $2D_s$, and $10D_s$ to illustrate the sensitivity of the triggering front to the estimate of the seismic diffusivity.

4 Case Study: Soultz-sous-Forêts

Numerous studies of IIS have previously indicated that tracking the location of the triggering front as observed in r-t plots may produce reasonable estimates of the effective hydraulic diffusivity at the injection site, mostly using the approach described by Shapiro et al. (1997) (Antonioli et al., 2005; Chen et al., 2012; Delepine et al., 2004; Goebel et al., 2017; Goertz-Allmann et al., 2017; Haffener et al., 2018; Hummel & Müller, 2009; Hummel & Shapiro, 2012, 2013; Ingebritsen & Manning, 2010; Improta et al., 2015; Rothert & Shapiro, 2003; Segall & Lu, 2015; Shapiro & Müller, 1999; Shapiro et al., 2002; Shapiro & Dinske, 2009a, 2009b; Yong et al., 2018; Yu et al., 2019). Although these previous studies have implicitly assumed that the seismic diffusivity is essentially equivalent to the effective hydraulic diffusivity, the numerical study presented here has clearly shown that these two quantities are likely distinct in heterogeneous domains. To further illustrate this potential distinction, we analyze the seismic dataset collected during the fluid injection experiment near Soultz-sous-Forêts, France in the year 2000.

The lower reservoir of the enhanced geothermal system (EGS) site near Soultz-sous-Forêts, France consists of three wells (called GPK2, GPK3, and GPK4) located in a highly fractured, crystalline rock formation approximately 4,000 - 5,000 meters below the ground surface (Dezayes et al., 2010; Genter et al., 2010; Meller & Ledésert, 2017). The site was selected for EGS due to the presence of a thermal anomaly, with downhole temperatures reaching 200° C in each of the three wells (Meller & Ledésert, 2017). Hydraulic stimulation was performed at each well at different times during the construction of the EGS site: GPK2 in 2000, GPK3 in 2003, and GPK4 in 2004 and 2005 (Dorbath et al., 2009; Meller & Ledésert, 2017). A full description of the site geology and wellbore details are given by Meller and Ledésert (2017) and Dezayes et al. (2010). Fluid injection and seismicity data have been presented by Genter et al. (2010) and Cuenot et al. (2008), in addition to being freely available through the EPOS-IP Anthropogenic Hazards data repository (Leptokaropoulos et al., 2019). Here, we present a case study of the fluid injection experiment performed at the GPK2 well in the year 2000.

Water was injected at an average rate of 44.6 liters per second (see Figure 16(a)) for a period of approximately six days. The screened interval of the injection well ranged from 4,400 to 5,100 meters below the ground surface. Using numerous surface and downhole seismometers, seismicity was tracked in space and time during the fluid injection experiment, which reached up to one kilometer away from the injection location. During just the first day of fluid injection, seismicity occurred as far as 700 meters away from the injection location. The r-t plot of this seismic dataset was shown earlier in Figure 1.

In order to characterize the hydraulic diffusivity of the EGS reservoir, Delepine et al. (2004) previously studied the spatiotemporal patterns of IIS found in this seismic dataset using the expression

$$r_t = \sqrt{4\pi D t} \tag{14}$$

which was originally suggested by Shapiro et al. (1997). By fitting equation (14) to the upper envelope of the seismic data cluster shown in Figure 16, the authors estimated the seismic diffusivity to be 0.15 m^2/s. (Note that the authors did not use the term "seismic diffusivity", but instead assume that the spatiotemporal patterns of IIS and the propagation of the triggering front is associated with the effective hydraulic diffusivity of the subsurface.) Equation (14) suggests that the triggering front propagates with $\sqrt{t}$ (Shapiro et al., 1997; Shapiro & Müller, 1999; Shapiro & Dinske, 2009b; Shapiro, 2015). This behavior is commonly found in IIS datasets and corresponds to a two-dimensional, diffusional process. The upper envelope of the seismic data cluster in Figure 16, though, appears to indicate a different behavior in the propagation of the triggering front. More complex triggering front behavior has been previously explained using nonlinear diffusion in two dimensions (Hummel & Shapiro, 2012, 2013; Shapiro & Dinske, 2009a, 2009b). While nonlinear diffusion may help to explain the triggering front behavior observed in this dataset (and its apparent deviation from the common $r_t \propto \sqrt{t}$ relationship), we suggest that the triggering front propagation is more appropriately described using a three-dimensional diffusion solution given by equation (13). The underlying porous medium is in fact three-dimensional and the diffusive propagation of the triggering front according to equation (13) does not necessarily conform to the $r_t \propto \sqrt{t}$ relationship and may therefore provide a better fit with the Soultz-sous-Forêts dataset. When fitting equation (13) to the upper envelope of the seismic data cluster (shown in Figure 16(b)), we assumed the fluid viscosity to be $2.0 \cdot 10^{-4}$ Pa $\cdot$ s to reflect water at approximately 200° C and the threshold triggering pressure increment to be 0.04 MPa, which is the minimum value used by Keranen et al. (2014) and well within the range suggested by others (Dempsey & Riffault, 2019; Gischig & Wiemer, 2013; Goebel et al., 2017; Shapiro, 2015).

The triggering front according to equation (13) fits the upper envelope of the seismic data cluster more accurately than equation (14). Notice that the rapid spread of seismicity during early times is captured well by equation (13) while underestimated by equation (14). The propagation rate of the triggering front at late time appears to be properly estimated by equation (13) as well. To evaluate the fit of each expression, we calculated both NRMSE and the NSE for equations (13) and (14). The reference dataset for the location of the triggering front was found by first binning the data into time periods of 0.1 days and then using the 10% of seismic events that occurred farthest away from the injection location within each time period. This set of seismic events are highlighted in Figure 16(b) in dark grey for reference. The NRMSE for equations (13) and (14) are 0.05 and 0.09 respectively. The NSE for equations (13) and (14) are 0.56 and -0.42 respectively. This indicates that equation (13) is a considerably better fit to the observed data than equation (14), and may therefore describe the propagation of the trig-

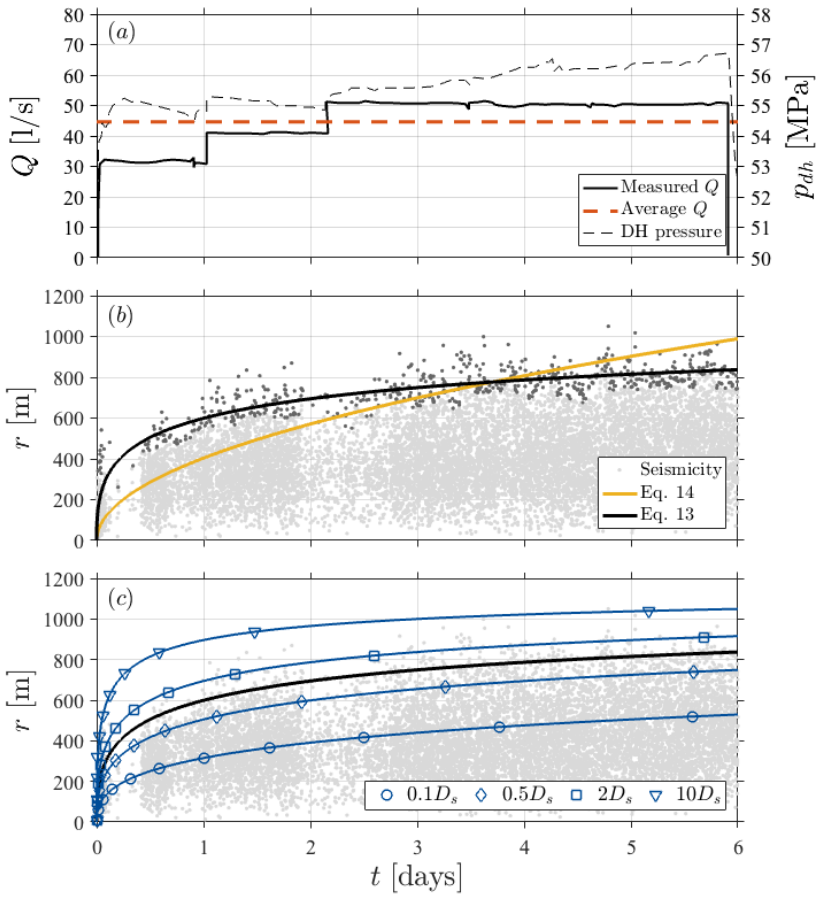

Figure 16. (a) Injection rate (Q) and downhole injection pressure (p_{dh}) from the fluid injection experiment near Soultz-sous-Forêts, France, with the calculated average injection rate overlaid. (b) The r-t plot for the fluid injection experiment. The seismic events are shown as light grey dots, with the farthest 10% of seismic events that occurred in each 0.1 day period plotted in dark grey (which were used to evaluate the fit of equation (13)). The seismic dataset has been fit with two expressions for the location of triggering front: (yellow) equation (14) using the diffusivity value of 0.15 m^2/s (Delepine et al., 2004) giving a normalized-root-mean-square-error of 0.09 and a Nash-Sutcliffe model efficiency coefficient of -0.42 and (black) equation (13) using the diffusivity value of 4.6 m^2/s giving a normalized-root-mean-square-error of 0.05 and a Nash-Sutcliffe model efficiency coefficient fo 0.56. (c) The r-t plot is overlaid with equation (13) using the estimated value of seismic diffusivity (D_s) as well as $0.1D_s$, $0.5D_s$, $2D_s$, and $10D_s$ to illustrate the degree of uncertainty in the estimate of seismic diffusivity using equation (13).

gering front more accurately and produce a more reliable estimate of seismic diffusivity.

For the Soultz-sous-Forêts dataset, the best estimate of seismic diffusivity is found to be 4.6 m^2/s according to the fit of equation (13) shown in Figure 16(b). To evaluate the potential uncertainty related to this estimate of seismic diffusivity, we plot the location of the triggering front according equation (13) using the estimated value of seismic diffusivity (D_s) as well as $0.1D_s$, $0.5D_s$, $2D_s$, and $10D_s$ in Figure 16(c). Visual inspection indicates that the triggering front fits the upper envelope of the seismic data cluster using seismic diffusivity values ranging between $0.5D_s$ and $2D_s$ (i.e. 2.3 m^2/s and 9.2 m^2/s). Note that the estimated value of seismic diffusivity depends on the set of seismic events selected when fitting the location of the triggering front. Here, we have elected to use the 10% of events that occurred the farthest away from the injection location within each time period. Of course, an alternative set (such as the farthest 5% or even 1% of seismic events) would produce different estimates of the seismic diffusivity, where sets of seismic events located farther from the injection location would naturally produce larger estimates of seismic diffusivity. Our final estimate of 4.6 m^2/s, then, represents a conservatively low estimate of the seismic diffusivity.

Other studies have attempted to characterize the subsurface in the vicinity of the GPK2 well (producing estimates of effective permeability) using various approaches including a laboratory experiment on core samples (Hettkamp et al., 1998), a pre-stimulation slug test (Weidler, 2001), an inverse modeling study using downhole pressure and injection rate data (McClure & Horne, 2011), a circulation test between wells GPK2 and GPK3 (Ledésert & Hébert, 2012), and a tracer experiment between wells GPK2, GPK3 and GPK4 (Vogt et al., 2012). To compare our value of seismic diffusivity to these studies, we first convert the estimates of effective permeability to effective hydraulic diffusivity using equation (2). For this, we assume that viscosity of the injected water at 200° C is $\mu = 2.0 \cdot 10^{-4}$ Pa · s, the porosity of the fractured, crystalline rock formation is $\phi = 0.05$ (Freeze & Cherry, 1987), and the typical value for the compressibility of water is $\beta_f = 4.4 \cdot 10^{-10}$ Pa^{-1}. For the bulk compressibility of the fractured crystalline rock (β_m), Vogt et al. (2012) employs a value of 10^{-8} Pa^{-1} while Freeze and Cherry (1987) report typical values ranging between 10^{-10} Pa^{-1} and 10^{-8} Pa^{-1}, where values less than 10^{-10} Pa^{-1} pertain to intact crystalline rock. Here, we use a value of 10^{-8} Pa^{-1} when converting to effective hydraulic diffusivity for the estimate associated with Vogt et al. (2012). For the other studies, we estimate a range of effective hydraulic diffusivity using the end member values of bulk compressibility reported by Freeze and Cherry (1987). The resulting estimates of effective hydraulic diffusivity from each study are shown in Table 4.

Comparing the value of seismic diffusivity found in this study (i.e. 4.6 m^2/s) to the values of effective hydraulic diffusivity given in Table 4, it is clear that the seismic diffusivity is one to five orders of magnitude larger than the effective hydraulic diffusivity. This case study thus provides potential empirical evidence suggesting that the seismic diffusivity associated with spatiotemporal patterns of IIS is distinct from the effective

Table 4. Estimates of the hydraulic diffusivity from various previous studies. Ranges shown here account for the broad range in the bulk compressibility of fractured rock (β_m) (Freeze & Cherry, 1987).

Study	Effective Hydraulic Diffusivity [m^2/s]
Hettkamp et al. (1998)	$1.9 \cdot 10^{-4}$ - $1.5 \cdot 10^{-2}$
Weidler (2001)	$2.5 \cdot 10^{-5}$ - $5.3 \cdot 10^{-3}$
McClure and Horne (2011)	$5.0 \cdot 10^{-3}$ - $4.1 \cdot 10^{-1}$
Ledésert and Hébert (2012)	$5.0 \cdot 10^{-4}$ - $4.1 \cdot 10^{-1}$
Vogt et al. (2012)	$5.0 \cdot 10^{-3}$

hydraulic diffusivity in heterogeneous porous media, such as the highly fractured, crystalline rock formation at the Soultz-sous-Forêts EGS site.

5 Conclusions and Discussion

In this paper, we analyzed the difference between the diffusivities associated with the propagation of seismicity (i.e. the seismic diffusivity) versus mean pressure diffusion (i.e. the effective hydraulic diffusivity) in heterogeneous subsurface formations. Often, the spatiotemporal patterns of IIS are interpreted with r-t plots and the concept of a triggering front, which has been previously shown to propagate in a diffusion-like manner with an associated diffusivity parameter (Segall & Lu, 2015; Shapiro et al., 1997; Shapiro, 2015). Here, we refer to this diffusivity as the "seismic diffusivity" following the terminology of Talwani and Acree (1985). If we assume that the onset of seismicity is induced by a threshold triggering pressure increment (p_t) (Dempsey & Riffault, 2019; Gischig & Wiemer, 2013; Goebel et al., 2017; Keranen et al., 2014; Shapiro, 2015), then the seismic diffusivity is associated with the spatiotemporal evolution of the farthest radial distance to which the threshold triggering pressure increment has propagated (i.e. $r_{max}(p = p_t)$). It is well established that effective hydraulic properties such as the effective hydraulic conductivity and effective hydraulic diffusivity describe the behavior of mean pressure fields (i.e. p_{avg}) in heterogeneous porous media (Dagan, 1989; Gelhar, 1993; Sanchez-Vila et al., 2006; Zhang, 2001). In a homogeneous porous medium, the seismic diffusivity is undoubtedly equivalent to the effective hydraulic diffusivity. However, due to the rapid preferential propagation of pressure increments through pathways of relatively high hydraulic diffusivity, this equivalence is not expected to hold in heterogeneous subsurface formations, since the propagation of $r_{max}(p = p_t)$ and $r(p_{avg} = p_t)$ are unlikely to coincide.

We have presented numerical simulations of fluid injection and IIS in heterogeneous domains in order to investigate the possible distinction between the seismic and effective hydraulic diffusivity. The fluid flow model (based on uncoupled, linear pressure dif-

fusion) simulated IIS by evaluating the Mohr-Coulomb failure criterion at randomly seeded weak points throughout the domain. We considered two forms of subsurface heterogeneity: spatially correlated, random fields of hydraulic diffusivity (i.e. the SGS domains) and highly fractured, low permeability rock (i.e. the DFNM domain). Results of the SGS simulations show that the location of $r_{max}(p = p_t)$ does indeed exceed $r(p_{avg} = p_t)$ in all cases at all times, with the distance between them increasing with the variability in the hydraulic permeability. Thus, we found that the seismic diffusivity (which describes the propagation of $r_{max}(p = p_t)$ and the spatiotemporal patterns of IIS) is in fact distinct from and greater than the effective hydraulic diffusivity of the SGS domains. After calculating the seismic diffusivity (D_s) and effective hydraulic diffusivity (D_{eff}) of each SGS domain, we found that the ratio D_s/D_{eff} was always above one and systematically increased with the degree of heterogeneity (i.e. with Var(lnκ)). For the largest value of Var(lnκ) considered (i.e. 5.3), the ratio D_s/D_{eff} had an ensemble mean of approximately 1.9 and the maximum value encountered in any realization was approximately 3.4. In contrast, results of the injection simulations in the DFNM domain found that the ratio D_s/D_{eff} was approximately 10.2, showing an order of magnitude difference between the seismic diffusivity and effective hydraulic diffusivity. The fracture network in the DFNM domain provides well-connected pathways of relatively high hydraulic diffusivity through which pressure increments can rapidly propagate. Moreover, we compared the DFNM simulation results to those from a homogeneous domain with the effective hydraulic properties of the DFNM domain. As expected, we found that the triggering front propagates much more rapidly in the DFNM domain and thus the equivalent homogeneous domain underestimates the extent of the seismically active region during fluid injection.

Overall, the results of this study indicate that the influence of subsurface heterogeneity creates spatiotemporal patterns of IIS that are not well described by the effective hydraulic diffusivity of the heterogeneous domain. Rather, the propagation of the triggering front and spatiotemporal patterns of IIS are controlled by the so-call seismic diffusivity (Talwani & Acree, 1985). This result suggests that estimates of hydraulic diffusivity from seismicity-based approaches (Delepine et al., 2004; Hummel & Müller, 2009; Hummel & Shapiro, 2012, 2013; Rothert & Shapiro, 2003; Segall & Lu, 2015; Shapiro et al., 1997; Shapiro & Müller, 1999; Shapiro et al., 2002; Shapiro & Dinske, 2009a, 2009b; Shapiro, 2015) likely over-estimate the true effective hydraulic diffusivity of the subsurface. Another critical implication is that modeling fluid injection operations with homogeneous domains using the effective hydraulic properties of the injection formation (Brown et al., 2017; Catalli et al., 2016; Dempsey & Riffault, 2019; Keranen et al., 2014; Langenbruch & Zoback, 2016; Langenbruch et al., 2018; Pollyea et al., 2019; Riffault et al., 2018) may underestimate the rate of propagation of seismicity and the size of the seismically active region. Alternatively, when employing the seismic diffusivity as a substitute for the effective hydraulic diffusivity, such models would produce the correct spatiotemporal patterns of IIS, yet other hydraulic processes may be inaccurately represented (such as inter-well connectivity or reservoir pressurization) (Birdsell et al., 2018; Haagenson et al., 2018; Haagenson & Rajaram, 2020).

Even if seismic diffusivity is not an accurate estimate of the effective hydraulic diffusivity in heterogeneous porous media, it may still be helpful by providing a simple descriptor of the rate at which seismicity appears to spread at a particular location. Since both the seismic diffusivity and the effective hydraulic diffusivity of subsurface formations are influenced by heterogeneity, estimation of the statistical properties of the underlying heterogeneity based on estimation of the seismic diffusivity may provide an indirect approach to estimating the effective hydraulic diffusivity. Conversely, hydraulic characterization at a particular site may indirectly provide estimates of the seismic diffusivity, allowing operators to evaluate the potential for the rapid propagation of seismicity.

Our approach involves approximations, which implies certain limitations. Foremost, the subsurface stress state is considered static during the simulation and only impacts the calculation of the Mohr-Coulomb failure criterion. This approach is similar to numerous previous studies that also neglect potential mechanical effects on the behavior of IIS (Brown et al., 2017; Dempsey & Riffault, 2019; Hummel & Shapiro, 2013; Keranen et al., 2014; Langenbruch et al., 2018; Nakai et al., 2017; Rothert & Shapiro, 2003; Shapiro et al., 1997, 2002; Shapiro & Dinske, 2009b; Shapiro, 2015; Talwani & Acree, 1985). Recently, there is a growing body of research investigating the influence of mechanical coupling on the behavior of IIS through both poroelastic stressing (Chang & Segall, 2016; Jha & Juanes, 2014; Rutqvist et al., 2013; Segall & Lu, 2015; Zhai & Shirzaei, 2018; Zhai et al., 2019) and static stress transfer following a seismic event (Catalli et al., 2016; Schoenball et al., 2012), which will certainly lead to improved insights on the physical nature of IIS phenomenon. In addition, we have neglected the dilation of fractures due to the change in normal effective stress (Bandis et al., 1983) or due to shear failure along a fracture (Rong et al., 2016; Ye & Ghassemi, 2018). We fully expect that including fracture dilation would only hasten the propagation of the triggering front and thus enhance the distinction between seismic diffusivity and the effective hydraulic diffusivity in formations of fractured rock. The influence of mechanical coupling is more difficult to predict, as changes to the stress state could be either stabilizing or destabilizing depending on the orientation of any given fracture. Future studies on this topic could investigate the potential influence of mechanical coupling or fracture dilation on the spatiotemporal behavior of IIS in three-dimensional domains of fractured rock. It may also be insightful to further explore the critical implications of the study's findings – particularly the potential for connecting the spatiotemporal patterns of IIS and estimates of the seismic diffusivity to various properties of the underlying fracture network. This could provide a highly beneficial tool for subsurface characterization or predicting the seismic response at potential fluid injection sites.

Acknowledgments

This work was financially supported by the National Science Foundation Hazards SEES project EAR 1520846 at the University of Colorado Boulder and Los Alamos National Laboratory (Center for Space and Earth Science and subcontract 437948 to the Univer-

sity of Colorado from LDRD Project 20170103DR). Work by this author was partially supported by the Department of Civil, Environmental, and Architectural Engineering at the University of Colorado Boulder through a Doctoral Assistantship for Completion of Dissertation. Also, we would like to thank Daniel Birdsell (now at ETH Zürich) for the numerous, insightful conversations about injection induced seismicity. Lastly, we would like to thank Jeffrey Hyman and Matthew Sweeney from Los Alamos National Laboratory for generously helping us implement dfnWorks in our project. The seismic dataset used in the case study of Soultz-sous-Forêts is freely available through the EPOS-IP Anthropogenic Hazards data repository (Leptokaropoulos et al., 2019).

References

Abushaikha, A. S., Blunt, M. J., Gosselin, O. R., Pain, C. C., & Jackson, M. D. (2015). Interface control volume finite element method for modelling multiphase fluid flow in highly heterogeneous and fractured reservoirs. *Journal of Computational Physics*, *298*, 41–61.

Adler, P. M., Thovert, J.-F., & Mourzenko, V. V. (2013). *Fractured porous media*. Oxford University Press.

Alnæs, M., Blechta, J., Hake, J., Johansson, A., Kehlet, B., Logg, A., ... Wells, G. N. (2015). The FEniCS project version 1.5. *Archive of Numerical Software*, *3*(100).

Antonioli, A., Piccinini, D., Chiaraluce, L., & Cocco, M. (2005). Fluid flow and seismicity pattern: Evidence from the 1997 Umbria-Marche (central Italy) seismic sequence. *Geophysical Research Letters*, *32*(10).

Bandis, S., Lumsden, A., & Barton, N. (1983). Fundamentals of rock joint deformation. In *International Journal of Rock Mechanics and Mining Sciences & Geomechanics Abstracts* (Vol. 20, pp. 249–268).

Bear, J. (1972). *Dynamics of fluids in porous media*.

Berre, I., Doster, F., & Keilegavlen, E. (2019). Flow in fractured porous media: A review of conceptual models and discretization approaches. *Transport in Porous Media*, *130*(1), 215–236.

Birdsell, D. T., Rajaram, H., Dempsey, D., & Viswanathan, H. S. (2015). Hydraulic fracturing fluid migration in the subsurface: A review and expanded modeling results. *Water Resources Research*, *51*(9), 7159–7188.

Birdsell, D. T., Rajaram, H., & Karra, S. (2018). Modeling Induced Seismicity with Fracture and Matrix Flow, Geomechanics, and Evolving Hydraulic Diffusivity. In *InterPore Annual Meeting and Jubilee.*

Botros, F. E., Hassan, A. E., Reeves, D. M., & Pohll, G. (2008). On mapping fracture networks onto continuum. *Water Resources Research*, *44*(8).

Bower, K., & Zyvoloski, G. (1997). A numerical model for thermo-hydro-mechanical coupling in fractured rock. *International Journal of Rock Mechanics and Mining Sciences*, *34*(8), 1201–1211.

Brezzi, F., Douglas, J., & Marini, L. D. (1985). Two families of mixed finite ele-

ments for second order elliptic problems. *Numerische Mathematik*, *47*(2), 217–235.

Brezzi, F., & Fortin, M. (2012). *Mixed and hybrid finite element methods* (Vol. 15). Springer Science & Business Media.

Brown, M. R., Ge, S., Sheehan, A. F., & Nakai, J. S. (2017). Evaluating the effectiveness of induced seismicity mitigation: Numerical modeling of wastewater injection near Greeley, Colorado. *Journal of Geophysical Research: Solid Earth*, *122*(8), 6569–6582.

Carslaw, H. S., & Jaeger, J. C. (1959). *Conduction of heat in solids*. Clarendon P.

Catalli, F., Rinaldi, A. P., Gischig, V., Nespoli, M., & Wiemer, S. (2016). The importance of earthquake interactions for injection-induced seismicity: Retrospective modeling of the Basel Enhanced Geothermal System. *Geophysical Research Letters*, *43*(10), 4992–4999.

Chang, K., & Segall, P. (2016). Injection-induced seismicity on basement faults including poroelastic stressing. *Journal of Geophysical Research: Solid Earth*, *121*(4), 2708–2726.

Chang, K., & Yoon, H. (2020). Hydromechanical Controls on the Spatiotemporal Patterns of Injection-Induced Seismicity in Different Fault Architecture: Implication for 2013–2014 Azle Earthquakes. *Journal of Geophysical Research: Solid Earth*, *125*(9), e2020JB020402.

Charbeneau, R. J. (2006). *Groundwater hydraulics and pollutant transport*. Waveland Press.

Chase, R. E., Liel, A. B., Luco, N., & Baird, B. W. (2019). Seismic loss and damage in light-frame wood buildings from sequences of induced earthquakes. *Earthquake Engineering & Structural Dynamics*, *48*(12), 1365–1383.

Chaudhuri, A., Rajaram, H., & Viswanathan, H. (2013). Early-stage hypogene karstification in a mountain hydrologic system: A coupled thermohydrochemical model incorporating buoyant convection. *Water Resources Research*, *49*(9), 5880–5899.

Chen, X., Shearer, P., & Abercrombie, R. (2012). Spatial migration of earthquakes within seismic clusters in Southern California: Evidence for fluid diffusion. *Journal of Geophysical Research: Solid Earth*, *117*(B4).

Chrysikopoulos, C. V. (1995). Effective parameters for flow in saturated heterogeneous porous media. *Journal of Hydrology*, *170*(1-4), 181–197.

Cleary, M. P. (1977). Fundamental solutions for a fluid-saturated porous solid. *International Journal of Solids and Structures*, *13*(9), 785–806.

Cuenot, N., Dorbath, C., & Dorbath, L. (2008). Analysis of the microseismicity induced by fluid injections at the EGS site of Soultz-sous-Forêts (Alsace, France): implications for the characterization of the geothermal reservoir properties. *Pure and Applied Geophysics*, *165*(5), 797–828.

Dagan, G. (1979). Models of groundwater flow in statistically homogeneous porous formations. *Water Resources Research*, *15*(1), 47–63.

Dagan, G. (1989). *Flow and transport in porous formations*. Springer Science &

Business Media.

Delepine, N., Cuenot, N., Rothert, E., Parotidis, M., Rentsch, S., & Shapiro, S. A. (2004). Characterization of fluid transport properties of the Hot Dry Rock reservoir Soultz-2000 using induced microseismicity. *Journal of Geophysics and Engineering*, *1*(1), 77–83.

De Marsily, G. (1986). *Quantitative hydrogeology*.

Dempsey, D., & Riffault, J. (2019). Response of induced seismicity to injection rate reduction: Models of delay, decay, quiescence, recovery, and Oklahoma. *Water Resources Research*, *55*(1), 656–681.

Deutsch, C., & Journel, A. (1998). Gslib-Geostatistical Software Library and User's Guide [Computer software manual]. Oxford University Press.

Dezayes, C., Genter, A., & Valley, B. (2010). Structure of the low permeable naturally fractured geothermal reservoir at Soultz. *Comptes Rendus Geoscience*, *342*(7-8), 517–530.

Dorbath, L., Cuenot, N., Genter, A., & Frogneux, M. (2009). Seismic response of the fractured and faulted granite of Soultz-sous-Forêts (France) to 5 km deep massive water injections. *Geophysical Journal International*, *177*(2), 653–675.

Dykaar, B. B., & Kitanidis, P. K. (1992a). Determination of the effective hydraulic conductivity for heterogeneous porous media using a numerical spectral approach: 1. Method. *Water Resources Research*, *28*(4), 1155–1166.

Dykaar, B. B., & Kitanidis, P. K. (1992b). Determination of the effective hydraulic conductivity for heterogeneous porous media using a numerical spectral approach: 2. Results. *Water Resources Research*, *28*(4), 1167–1178.

Ellsworth, W. L. (2013). Injection-induced earthquakes. *Science*, *341*(6142), 1225942.

EPA, U. (2016). *Hydraulic fracturing for oil and gas: Impacts from the hydraulic 325 fracturing water cycle on drinking water resources in the united states. Washington, DC: US Environmental Protection Agency* (Tech. Rep.). EPA/600/R-16.

Fernàndez-Garcia, D., Rajaram, H., & Illangasekare, T. H. (2005). Assessment of the predictive capabilities of stochastic theories in a three-dimensional laboratory test aquifer: Effective hydraulic conductivity and temporal moments of breakthrough curves. *Water Resources Research*, *41*(4).

Frampton, A., Hyman, J., & Zou, L. (2019). Advective transport in discrete fracture networks with connected and disconnected textures representing internal aperture variability. *Water Resources Research*, *55*(7), 5487–5501.

Freeze, R. A., & Cherry, J. A. (1987). Groundwater. *Prentice˜ Hall, Englewood I Cliffs, N.]., USA*, *12*, 145–165.

Fumagalli, A., & Scotti, A. (2013). A reduced model for flow and transport in fractured porous media with non-matching grids. In *Numerical Mathematics and Advanced Applications* (pp. 499–507). Springer.

Geiger, S., Cortis, A., & Birkholzer, J. (2010). Upscaling solute transport in naturally fractured porous media with the continuous time random walk method.

Water Resources Research, *46*(12).

Gelhar, L. W. (1993). *Stochastic subsurface hydrology* (Vol. 390). Prentice-Hall Englewood Cliffs, NJ.

Genter, A., Evans, K., Cuenot, N., Fritsch, D., & Sanjuan, B. (2010). Contribution of the exploration of deep crystalline fractured reservoir of Soultz to the knowledge of enhanced geothermal systems (EGS). *Comptes Rendus Geoscience*, *342*(7-8), 502–516.

Gischig, V. S., & Wiemer, S. (2013). A stochastic model for induced seismicity based on non-linear pressure diffusion and irreversible permeability enhancement. *Geophysical Journal International*, *194*(2), 1229–1249.

Goebel, T., Weingarten, M., Chen, X., Haffener, J., & Brodsky, E. (2017). The 2016 Mw5. 1 Fairview, Oklahoma earthquakes: Evidence for long-range poroelastic triggering at¿ 40 km from fluid disposal wells. *Earth and Planetary Science Letters*, *472*, 50–61.

Goertz-Allmann, B., Gibbons, S., Oye, V., Bauer, R., & Will, R. (2017). Characterization of induced seismicity patterns derived from internal structure in event clusters. *Journal of Geophysical Research: Solid Earth*, *122*(5), 3875–3894.

Guadagnini, A., Riva, M., & Neuman, S. P. (2003). Three-dimensional steady state flow to a well in a randomly heterogeneous bounded aquifer. *Water Resources Research*, *39*(3).

Gutjahr, A. L., Gelhar, L. W., Bakr, A. A., & MacMillan, J. R. (1978). Stochastic analysis of spatial variability in subsurface flows: 2. Evaluation and application. *Water Resources Research*, *14*(5), 953–959.

Haagenson, R., & Rajaram, H. (2020). Seismic diffusivity: The influence of fracture networks on the patterns of induced seismicity. In *EGU General Assembly Conference Abstracts* (p. 20308).

Haagenson, R., Rajaram, H., & Allen, J. (2020). A generalized poroelastic model using FEniCS with insights into the Noordbergum effect. *Computers & Geosciences*, *135*, 104399.

Haagenson, R., Rajaram, H., Karra, S., & Allen, J. (2018). Modeling Nonlinear Diffusion in Fractured Rock With Deformable Fractures and Applications To Injection Induced Seismicity. In *2nd International Discrete Fracture Network Engineering Conference.*

Haffener, J., Chen, X., & Murray, K. (2018). Multiscale analysis of spatiotemporal relationship between injection and seismicity in Oklahoma. *Journal of Geophysical Research: Solid Earth*, *123*(10), 8711–8731.

Hajati, T., Langenbruch, C., & Shapiro, S. (2015). A statistical model for seismic hazard assessment of hydraulic-fracturing-induced seismicity. *Geophysical Research Letters*, *42*(24), 10–601.

Healy, J., Rubey, W., Griggs, D., & Raleigh, C. (1968). The denver earthquakes. *Science*, *161*(3848), 1301–1310.

Hettkamp, T., Klee, G., & Rummel, F. (1998). Stress regime and permeability at Soultz derived from the laboratory and in situ tests. In *Draft Proceedings 4th*

International HDR Forum.

Hummel, N., & Müller, T. (2009). Microseismic signatures of non-linear pore-fluid pressure diffusion. *Geophysical Journal International*, *179*(3), 1558–1565.

Hummel, N., & Shapiro, S. (2012). Microseismic estimates of hydraulic diffusivity in case of non-linear fluid-rock interaction. *Geophysical Journal International*, *188*(3), 1441–1453.

Hummel, N., & Shapiro, S. A. (2013). Nonlinear diffusion-based interpretation of induced microseismicity: A Barnett Shale hydraulic fracturing case studyNonlinear diffusion and fracturing of shales. *Geophysics*, *78*(5), B211–B226.

Hyman, J., Painter, S. L., Viswanathan, H., Makedonska, N., & Karra, S. (2015). Influence of injection mode on transport properties in kilometer-scale three-dimensional discrete fracture networks. *Water Resources Research*, *51*(9), 7289–7308.

Hyman, J. D., Karra, S., Makedonska, N., Gable, C. W., Painter, S. L., & Viswanathan, H. S. (2015). dfnWorks: A discrete fracture network framework for modeling subsurface flow and transport. *Computers & Geosciences*, *84*, 10–19.

Improta, L., Valoroso, L., Piccinini, D., & Chiarabba, C. (2015). A detailed analysis of wastewater-induced seismicity in the Val d'Agri oil field (Italy). *Geophysical Research Letters*, *42*(8), 2682–2690.

Ingebritsen, S. E., & Manning, C. (2010). Permeability of the continental crust: dynamic variations inferred from seismicity and metamorphism. *Geofluids*, *10*(1-2), 193–205.

Jaeger, J. (1959). The frictional properties of joints in rock. *Geofisica Pura e Applicata*, *43*(1), 148–158.

Jha, B., & Juanes, R. (2014). Coupled multiphase flow and poromechanics: A computational model of pore pressure effects on fault slip and earthquake triggering. *Water Resources Research*, *50*(5), 3776–3808.

Keranen, K. M., Weingarten, M., Abers, G. A., Bekins, B. A., & Ge, S. (2014). Sharp increase in central Oklahoma seismicity since 2008 induced by massive wastewater injection. *Science*, *345*(6195), 448–451.

Langenbruch, C., Weingarten, M., & Zoback, M. D. (2018). Physics-based forecasting of man-made earthquake hazards in Oklahoma and Kansas. *Nature Communications*, *9*(1), 1–10.

Langenbruch, C., & Zoback, M. D. (2016). How will induced seismicity in Oklahoma respond to decreased saltwater injection rates? *Science Advances*, *2*(11), e1601542.

Ledésert, B. A., & Hébert, R. L. (2012). The Soultz-sous-Forêts enhanced geothermal system: a granitic basement used as a heat exchanger to produce electricity. *Heat Exchanges—Basic Design Applications*, 477–504.

Leptokaropoulos, K., Cielesta, S., Staszek, M., Olszewska, D., Lizurek, G., Kocot, J., ... Szepieniec, T. (2019). IS-EPOS: a platform for anthropogenic seismicity research. *Acta Geophysica*, *67*(1), 299–310.

Long, J., Remer, J., Wilson, C., & Witherspoon, P. (1982). Porous media equivalents for networks of discontinuous fractures. *Water Resources Research*, *18*(3), 645–658.

Majer, E., Nelson, J., Robertson-Tait, A., Savy, J., & Wong, I. (2012). Protocol for addressing induced seismicity associated with enhanced geothermal systems. *US Department of Energy*, 52.

McClure, M. W., & Horne, R. N. (2011). Pressure transient analysis of fracture zone permeability at Soultz-sous-Forêts. *GRC Transactions*, *35*, 1487.

Meller, C., & Ledésert, B. (2017). Is there a link between mineralogy, petrophysics, and the hydraulic and seismic behaviors of the Soultz-sous-Forêts granite during stimulation? A review and reinterpretation of petro-hydromechanical data toward a Better" Understanding of Induced Seismicity and Fluid Flow. *Journal of Geophysical Research: Solid Earth*, *122*(12), 9755–9774.

Müller, S., & Schüler, L. (2020, Apr). *GeoStat-Framework/GSTools: Volatile Violet v1.2.1.* Retrieved from `https://zenodo.org/record/3751743`

Murphy, H., Huang, C., Dash, Z., Zyvoloski, G., & White, A. (2004). Semianalytical solutions for fluid flow in rock joints with pressure-dependent openings. *Water Resources Research*, *40*(12).

Naff, R. (1991). Radial flow in heterogeneous porous media: An analysis of specific discharge. *Water Resources Research*, *27*(3), 307–316.

Nakai, J., Weingarten, M., Sheehan, A., Bilek, S., & Ge, S. (2017). A possible causative mechanism of Raton Basin, New Mexico and Colorado earthquakes using recent seismicity patterns and pore pressure modeling. *Journal of Geophysical Research: Solid Earth*, *122*(10), 8051–8065.

Odsæter, L. H., Kvamsdal, T., & Larson, M. G. (2019). A simple embedded discrete fracture–matrix model for a coupled flow and transport problem in porous media. *Computer Methods in Applied Mechanics and Engineering*, *343*, 572–601.

Paleologos, E. K., Neuman, S. P., & Tartakovsky, D. (1996). Effective hydraulic conductivity of bounded, strongly heterogeneous porous media. *Water Resources Research*, *32*(5), 1333–1341.

Pandey, S., Chaudhuri, A., & Kelkar, S. (2017). A coupled thermo-hydro-mechanical modeling of fracture aperture alteration and reservoir deformation during heat extraction from a geothermal reservoir. *Geothermics*, *65*, 17–31.

Pandey, S., & Rajaram, H. (2016). Modeling the influence of preferential flow on the spatial variability and time-dependence of mineral weathering rates. *Water Resources Research*, *52*(12), 9344–9366.

Pollyea, R. M., Chapman, M. C., Jayne, R. S., & Wu, H. (2019). High density oilfield wastewater disposal causes deeper, stronger, and more persistent earthquakes. *Nature Communications*, *10*(1), 1–10.

Renard, P., & De Marsily, G. (1997). Calculating equivalent permeability: a review. *Advances in Water Resources*, *20*(5-6), 253–278.

Rice, J. R., & Cleary, M. P. (1976). Some basic stress diffusion solutions for fluid-saturated elastic porous media with compressible constituents. *Reviews of Geo-*

physics, *14*(2), 227–241.

Riffault, J., Dempsey, D., Karra, S., & Archer, R. (2018). Microseismicity cloud can be substantially larger than the associated stimulated fracture volume: the case of the Paralana Enhanced Geothermal System. *Journal of Geophysical Research: Solid Earth*, *123*(8), 6845–6870.

Rinaldi, A. P., & Nespoli, M. (2017). TOUGH2-seed: A coupled fluid flow and mechanical-stochastic approach to model injection-induced seismicity. *Computers & Geosciences*, *108*, 86–97.

Rong, G., Yang, J., Cheng, L., & Zhou, C. (2016). Laboratory investigation of nonlinear flow characteristics in rough fractures during shear process. *Journal of Hydrology*, *541*, 1385–1394.

Rothert, E., & Shapiro, S. A. (2003). Microseismic monitoring of borehole fluid injections: Data modeling and inversion for hydraulic properties of rocks. *Geophysics*, *68*(2), 685–689.

Rudnicki, J. W. (1986). Fluid mass sources and point forces in linear elastic diffusive solids. *Mechanics of Materials*, *5*(4), 383–393.

Rutqvist, J., Cappa, F., Rinaldi, A. P., & Godano, M. (2014). Modeling of induced seismicity and ground vibrations associated with geologic CO2 storage, and assessing their effects on surface structures and human perception. *International Journal of Greenhouse Gas Control*, *24*, 64–77.

Rutqvist, J., Noorishad, J., Tsang, C.-F., & Stephansson, O. (1998). Determination of fracture storativity in hard rocks using high-pressure injection testing. *Water Resources Research*, *34*(10), 2551–2560.

Rutqvist, J., Rinaldi, A. P., Cappa, F., & Moridis, G. J. (2013). Modeling of fault reactivation and induced seismicity during hydraulic fracturing of shale-gas reservoirs. *Journal of Petroleum Science and Engineering*, *107*, 31–44.

Sanchez-Vila, X., Guadagnini, A., & Carrera, J. (2006). Representative hydraulic conductivities in saturated groundwater flow. *Reviews of Geophysics*, *44*(3).

Schoenball, M., Baujard, C., Kohl, T., & Dorbath, L. (2012). The role of triggering by static stress transfer during geothermal reservoir stimulation. *Journal of Geophysical Research: Solid Earth*, *117*(B9).

Segall, P., & Lu, S. (2015). Injection-induced seismicity: Poroelastic and earthquake nucleation effects. *Journal of Geophysical Research: Solid Earth*, *120*(7), 5082–5103.

Shapiro, S. A. (2015). *Fluid-induced seismicity*. Cambridge University Press.

Shapiro, S. A., & Dinske, C. (2009a). Fluid-induced seismicity: Pressure diffusion and hydraulic fracturing. *Geophysical Prospecting*, *57*(2), 301–310.

Shapiro, S. A., & Dinske, C. (2009b). Scaling of seismicity induced by nonlinear fluid-rock interaction. *Journal of Geophysical Research: Solid Earth*, *114*(B9).

Shapiro, S. A., Huenges, E., & Borm, G. (1997). Estimating the crust permeability from fluid-injection-induced seismic emission at the KTB site. *Geophysical Journal International*, *131*(2), F15–F18.

Shapiro, S. A., & Müller, T. M. (1999). Seismic signature of permeability in heterogeneous porous media. *Geophysics*, *64*(1), 99–103.

Shapiro, S. A., Rentsch, S., & Rothert, E. (2005). Characterization of hydraulic properties of rocks using probability of fluid-induced microearthquakes. *Geophysics*, *70*(2), F27–F33.

Shapiro, S. A., Rothert, E., Rath, V., & Rindschwentner, J. (2002). Characterization of fluid transport properties of reservoirs using induced microseismicity. *Geophysics*, *67*(1), 212–220.

Sweeney, M. R., Gable, C. W., Karra, S., Stauffer, P. H., Pawar, R. J., & Hyman, J. D. (2020). Upscaled discrete fracture matrix model (UDFM): an octree-refined continuum representation of fractured porous media. *Computational Geosciences*, *24*(1), 293–310.

Talwani, P., & Acree, S. (1985). Pore pressure diffusion and the mechanism of reservoir-induced seismicity. In *Earthquake Prediction* (pp. 947–965). Springer.

Tompson, A. F., Ababou, R., & Gelhar, L. W. (1989). Implementation of the three-dimensional turning bands random field generator. *Water Resources Research*, *25*(10), 2227–2243.

Traverso, L., Phillips, T. N., & Yang, Y. (2013). Mixed finite element methods for groundwater flow in heterogeneous aquifers. *Computers & Fluids*, *88*, 60–80.

Verruijt, A. (2013). *Theory and Problems of Poroelasticity*.

Vogt, C., Marquart, G., Kosack, C., Wolf, A., & Clauser, C. (2012). Estimating the permeability distribution and its uncertainty at the EGS demonstration reservoir Soultz-sous-Forêts using the ensemble Kalman filter. *Water Resources Research*, *48*(8).

Weidler, R. (2001). Slug test in the non-stimulated 5 km deep well GPK2. *Internal BGR report, Hannover, Germany*.

Weingarten, M., Ge, S., Godt, J. W., Bekins, B. A., & Rubinstein, J. L. (2015). High-rate injection is associated with the increase in US mid-continent seismicity. *Science*, *348*(6241), 1336–1340.

Wen, X.-H., & Gómez-Hernández, J. J. (1996). Upscaling hydraulic conductivities in heterogeneous media: An overview. *Journal of Hydrology*, *183*(1-2), ix–xxxii.

Ye, Z., & Ghassemi, A. (2018). Injection-induced shear slip and permeability enhancement in granite fractures. *Journal of Geophysical Research: Solid Earth*, *123*(10), 9009–9032.

Yong, Y. K., Maulianda, B., Wee, S. C., Mohshim, D., Elraies, K. A., Wong, R. C., ... Eaton, D. (2018). Determination of stimulated reservoir volume and anisotropic permeability using analytical modelling of microseismic and hydraulic fracturing parameters. *Journal of Natural Gas Science and Engineering*, *58*, 234–240.

Younes, A., Ackerer, P., & Delay, F. (2010). Mixed finite elements for solving 2-D diffusion-type equations. *Reviews of Geophysics*, *48*(1).

Yu, H., Harrington, R., Liu, Y., & Wang, B. (2019). Induced Seismicity Driven

by Fluid Diffusion Revealed by a Near-Field Hydraulic Stimulation Monitoring Array in the Montney Basin, British Columbia. *Journal of Geophysical Research: Solid Earth*, *124*(5), 4694–4709.

Zhai, G., & Shirzaei, M. (2018). Fluid injection and time-dependent seismic hazard in the Barnett Shale, Texas. *Geophysical Research Letters*, *45*(10), 4743–4753.

Zhai, G., Shirzaei, M., Manga, M., & Chen, X. (2019). Pore-pressure diffusion, enhanced by poroelastic stresses, controls induced seismicity in Oklahoma. *Proceedings of the National Academy of Sciences*, *116*(33), 16228–16233.

Zhang, D. (2001). *Stochastic methods for flow in porous media: coping with uncertainties*. Elsevier.

Zimmerman, R., & Bodvarsson, G. (1996). Effective transmissivity of two-dimensional fracture networks. *International Journal of Rock Mechanics and Mining Sciences & Geomechanics Abstracts*, *33*(4), 433 - 438.

Zimmerman, R. W., & Bodvarsson, G. S. (1996). Hydraulic conductivity of rock fractures. *Transport in Porous Media*, *23*(1), 1–30.

Zoback, M. D. (2010). *Reservoir geomechanics*. Cambridge University Press.